DRAFT VERSION AUGUST 11, 2026
Typeset using LATEX **twocolumn** style in AASTeX63

GATOS: Distinct Feedback Modes in AGN Central Regions Revealed by Spatially Resolved JWST Spectroscopy

LULU ZHANG,[1] CHRIS PACKHAM,[1,2] ERIN K. S. HICKS,[3,1,4] ISMAEL GARCÍA-BERNETE,[5]
ALMUDENA ALONSO-HERRERO,[5] RIC I. DAVIES,[6] MARTIN J. WARD,[7] DANIEL E. DELANEY,[4,3] TAKUMA IZUMI,[2,8]
DIMITRA RIGOPOULOU,[9,10] CRISTINA RAMOS ALMEIDA,[11,12] OMAIRA GONZÁLEZ-MARTÍN,[13] ROGEMAR A. RIFFEL,[14]
CLAUDIO RICCI,[15,16] MONTSERRAT VILLAR-MARTÍN,[17] FRANCOISE COMBES,[18] MIGUEL PEREIRA-SANTAELLA,[19]
SEBASTIAN F. HOENIG,[20] ANDREW J. BUNKER,[9] PETER G. BOORMAN,[6] ENRICA BELLOCCHI,[21,22]
NANCY A. LEVENSON,[23] SANTIAGO GARCÍA-BURILLO,[24] FERGUS R. DONNAN,[25] ANELISE AUDIBERT,[11,12]
LINDSAY FULLER,[1] TANIO DÍAZ-SANTOS,[26,10] AND DAVID J. ROSARIO[27]

[1]*The University of Texas at San Antonio, One UTSA Circle, San Antonio, TX 78249, USA; lulu.zhang@utsa.edu; l.l.zhangastro@gmail.com*
[2]*National Astronomical Observatory of Japan, National Institutes of Natural Sciences (NINS), 2-21-1 Osawa, Mitaka, Tokyo 181-8588, Japan*
[3]*Department of Physics and Astronomy, University of Alaska Anchorage, Anchorage, AK 99508-4664, USA*
[4]*Department of Physics, University of Alaska, Fairbanks, Alaska 99775-5920, USA*
[5]*Centro de Astrobiología (CAB), CSIC-INTA, Camino Bajo del Castillo s/n, E-28692 Villanueva de la Cañada, Madrid, Spain*
[6]*Max-Planck-Institut für extraterrestrische Physik, Postfach 1312, D-85741, Garching, Germany*
[7]*Centre for Extragalactic Astronomy, Durham University, South Road, Durham DH1 3LE, UK*
[8]*Department of Astronomy, School of Science, Graduate University for Advanced Studies (SOKENDAI), Mitaka, Tokyo 181-8588, Japan*
[9]*Department of Physics, University of Oxford, Keble Road, Oxford OX1 3RH, UK*
[10]*School of Sciences, European University Cyprus, Diogenes street, Engomi, 1516 Nicosia, Cyprus*
[11]*Instituto de Astrofísica de Canarias, Calle Vía Láctea, s/n, E-38205, La Laguna, Tenerife, Spain*
[12]*Departamento de Astrofísica, Universidad de La Laguna, E-38206, La Laguna, Tenerife, Spain*
[13]*Instituto de Radioastronomía and Astrofísica (IRyA-UNAM), 3-72 (Xangari), 8701, Morelia, Mexico*
[14]*Departamento de Física, CCNE, Universidade Federal de Santa Maria, Av. Roraima 1000, 97105-900, Santa Maria, RS, Brazil*
[15]*Department of Astronomy, University of Geneva, ch. d'Ecogia 16, 1290, Versoix, Switzerland*
[16]*Instituto de Estudios Astrofísicos, Facultad de Ingeniería y Ciencias, Universidad Diego Portales, Av. Ejército Libertador 441, Santiago, Chile*
[17]*Centro de Astrobiología (CAB), CSIC-INTA, Ctra. de Ajalvir km 4, Torrejón de Ardoz, E-28850, Madrid, Spain*
[18]*LUX, Observatoire de Paris, Collège de France, PSL University, CNRS, Sorbonne University, Paris*
[19]*Instituto de Física Fundamental, CSIC, Calle Serrano 123, 28006 Madrid, Spain*
[20]*School of Physics and Astronomy, University of Southampton, Southampton SO17 1BJ, UK*
[21]*Departamento de Física de la Tierra y Astrofísica, Fac. de CC. Físicas, Universidad Complutense de Madrid, 28040 Madrid, Spain*
[22]*Instituto de Física de Partículas y del Cosmos IPARCOS, Fac. CC. Físicas, Universidad Complutense de Madrid, 28040 Madrid, Spain*
[23]*Space Telescope Science Institute, 3700 San Martin Drive Baltimore, Maryland 21218, USA*
[24]*Observatorio Astronómico Nacional (OAN-IGN)-Observatorio de Madrid, Alfonso XII, 3, 28014, Madrid, Spain*
[25]*Department of Astronomy and Astrophysics, University of California, San Diego, La Jolla, CA 92093, USA*
[26]*Institute of Astrophysics, Foundation for Research and Technology-Hellas (FORTH), Heraklion 70013, Greece*
[27]*School of Mathematics, Statistics and Physics, Newcastle University, Newcastle upon Tyne, NE1 7RU, UK*

ABSTRACT

This manuscript presents JWST MIRI/MRS observations of the central $r \approx 40-240$ pc regions of five active galactic nuclei (AGN) spanning a wide range of luminosities ($\log L_{\rm bol}/{\rm erg\,s^{-1}} \approx$ 39.8–43.8). Combining multiphase diagnostics from polycyclic aromatic hydrocarbons (PAHs), molecular hydrogen (H_2), and ionized gas at spatial scales of $\sim$4–24 pc, this study presents a spatially resolved investigation into the effects of the two distinct AGN feedback modes–radiative and kinetic–on the surrounding medium. The results indicate that these two feedback modes, associated with AGN irradiation and shock processing, respectively, collectively drive the relative suppression of PAH emission in the nuclear regions of the targets studied here. Moreover, the coexistence of these two AGN feedback modes, especially the shock processing associated with either jets or outflows, in the central regions of AGN naturally explains both the bimodal distribution of PAH band ratios observed in the targets studied here and the seemingly disparate results reported in the literature. Although based on a limited sample, these findings provide new insights into calibrating star-formation rates (SFRs) from PAH emission in AGN, and more importantly, lay the groundwork for a practical framework to diagnose and quantify AGN feedback in the JWST era.

Keywords: galaxies: active galactic nucleus — galaxies: ISM — infrared: ISM — galaxies: star formation

1. INTRODUCTION

The co-evolution of supermassive black holes (SMBHs) and their host galaxies–a central paradigm in modern extragalactic astrophysics (for a review see Kormendy & Ho 2013)–requires the injection of substantial energy and momentum from active galactic nuclei (AGN)–the observable phases of SMBH accretion–into the surrounding interstellar medium (ISM) (for reviews see Silk & Rees 1998; Fabian 2012). In observation, this injection–commonly referred to as AGN feedback–manifests in two primary modes, widely termed the "radiative" (or quasar) mode and the "kinetic" (or radio) mode (for a review see Alexander & Hickox 2012).

The radiative mode is typically associated with luminous AGN, whose intense radiation efficiently expels the surrounding gas (e.g., Di Matteo et al. 2005; Hopkins et al. 2008), driving multiphase outflows detected across a broad range of wavelengths, including ionized gas traced by UV-optical-infared emission lines, warm molecular gas in the infrared, and cold molecular gas in millimeter wavelengths (e.g., Cicone et al. 2014; Davies et al. 2014, 2024; Fiore et al. 2017; Fluetsch et al. 2019; Ramos Almeida et al. 2022; Esposito et al. 2024; Zhang et al. 2024a; Bellocchi et al. 2026; and for a review see Harrison & Ramos Almeida 2024). In contrast, the kinetic mode is more prevalent in low-luminosity AGN, which have extremely low radiative efficiencies (Ho et al. 2003; Ho 2009) and whose central engines are often dominated by jet power (e.g., Mezcua & Prieto 2014; Fernández-Ontiveros et al. 2012; Goold et al. 2026), heating the surrounding gas through shocks (e.g., Weinberger et al. 2017; and for reviews see McNamara & Nulsen 2007; Ho 2008). Direct evidence of such jet- and shock-driven feedback, including cavities, lobes, and shock fronts in hot gas, have been observed in radio and X-ray bands (e.g., McNamara & Nulsen 2007; Morganti et al. 2013a), with jet- and shock-ISM interaction signatures, including disturbed kinematics and enhanced excitation in cold and warm gas, been observed in optical, infrared, and millimeter bands (e.g., Morganti et al. 2013b; Nesvadba et al. 2017; Venturi et al. 2021; Audibert et al. 2023; Dasyra et al. 2024; Riffel et al. 2026b).

These two modes are proposed to reflect different accretion states and environmental couplings, yet both play a fundamental role in heating, redistributing, and transforming the ISM on galactic scales, thereby driving galaxy evolution (for reviews see Alexander & Hickox 2012; Heckman & Best 2014). A clear understanding of AGN feedback is therefore essential for placing meaningful constraints on models of galaxy formation and evolution. Correspondingly, state-of-the-art cosmological simulations increasingly rely on sub-grid prescriptions for AGN-driven energy injection to reproduce key observables, such as the galaxy stellar mass function, star formation histories, and atomic/molecular gas fractions (e.g., Crain et al. 2015; Pillepich et al. 2018; Davé et al. 2020). However, significant uncertainties remain regarding how AGN-released energy couples to different gas phases and the spatial and temporal scales over which feedback operates. In this context, detailed studies of nearby galaxies, through spatially resolved measurements of gas content, kinematics, excitation, and energetics, provide critical laboratories for addressing these uncertainties. Insights from the local studies can then be extrapolated to the high-redshift universe, where direct constraints are more limited, thereby informing our understanding of AGN feedback and its role in galaxy formation and evolution in the early universe.

The advent of JWST (Gardner et al. 2023) opens a new window for probing AGN feedback with unprecedented sensitivity and spectral coverage. Its IFU capabilities in the near- and mid-infrared enable spatially resolved, and joint, access to diagnostic features from multiple ionized, neutral, and molecular gas, as well as dust components, in local galaxies. Key spectral tracers, including fine-structure lines from ionized gas, rotational and ro-vibrational transitions of molecular hydrogen (H_2), and broad features from polycyclic aromatic hydrocarbon (PAH) molecules, are particularly sensitive to the heating and excitation processes associated with AGN activity (e.g., Davies et al. 2024; García-Bernete et al. 2024b; Alonso Herrero et al. 2025; López et al. 2025; Ramos Almeida et al. 2025; Goold et al. 2026; Hermosa Muñoz et al. 2026; Zhang et al. 2026). By capturing these signatures at high spatial and spectral resolution, JWST enables a comprehensive, multiphase characterization of feedback processes (e.g., Zhang & Ho 2023c; Zhang et al. 2024b, 2026 and references therein), yielding critical insights into how AGN shape their host galaxies and, in turn, drive galaxy evolution.

2. OBSERVATION AND ANALYSIS

2.1. *Targets and Observations*

The targets analyzed here comprise three low-ionization nuclear emission-line regions (LINERs) and two Seyfert galaxies, spanning a broad range of AGN luminosities ($L_{\rm bol} \approx 10^{39.8} - 10^{43.8}\,{\rm erg\,s^{-1}}$). These targets, unless otherwise specified in Table 1, are part of the Galaxy Activity, Torus, and Outflow Survey[1] (GATOS; e.g., Alonso-Herrero et al. 2021; García-Burillo et al. 2021, 2024). This study presents JWST spectroscopic observations of the two Seyfert

[1] https://gatos-astro.com

galaxies for the first time and performs a spatially resolved analysis of all five targets, including the three LINERs for which only nuclear integrated spectra have previously been analyzed (Zhang et al. 2026). These targets were selected for JWST programs predominantly based on their nuclear sub-kiloparsec-scale PAH properties, which span two regimes expected to arise from the primary modes of AGN feedback. Additionally, the three LINERs all show evidence of radio cores associated with AGN (Nagar et al. 2005; Nemmen et al. 2014), in contrast to the two Seyfert galaxies, which both exhibit prominent AGN ionization cones (Marconi et al. 1994; da Silva et al. 2023); NGC 7314 also hosts two off-nuclear radio spots (Thean et al. 2000). As such, they provide an ideal, albeit limited, sample for disentangling the roles of different AGN feedback mechanisms through the joint interpretation of PAH features and other infrared diagnostics.

Table 1. Basic Properties of the AGN Sample

Target	Hubble Type	AGN Type	z	D	scale	$cos(i)$	log $L_{\rm bol}$	log $M_{\rm BH}$	log $\lambda_{\rm Edd}$
(-)	(-)	(-)	(-)	(Mpc)	(pc/$''$)	(-)	[erg s^{-1}]	[M$_\odot$]	(-)
(1)	(2)	(3)	(4)	(5)	(6)	(7)	(8)	(9)	(10)
NGC 1097†	SBb	L/Sy	0.004240	17.2	80	0.68	42.0	8.1	−4.2
NGC 3190	Sa	L	0.004370	24.5	120	0.34	40.8	8.2	−5.5
NGC 4736*	Sab	L/Sy	0.001027	5.1	25	0.81	39.8	7.2	−5.5
NGC 7314‡	SABbc	Sy	0.004763	16.7	80	0.34	43.5	6.2	−0.8
Circinus Galaxy*	SAb	Sy	0.001448	4.2	20	0.42	43.8	6.2	−0.5

NOTE—Column (1-5): Target name, Hubble type, AGN type ("L" for LINER; "Sy" for Seyfert), redshift, and redshift-independent distance taken from the NASA/IPAC Extragalactic Database; Column (6): The linear scale corresponding to an angular size of 1 arcsec at the distance of each target. Column (7): Cosine value of the inclination angle on the galactic scale, taken as the ratio of the photometric minor to major axis, cos(i) = b/a, unless otherwise specified (Kennicutt et al. 2003; García-Burillo et al. 2021). Column (8): AGN bolometric luminosity $L_{\rm bol} = 15.8 \times L_{(2-10){\rm keV}}$, with the nuclear 2–10 keV X-ray luminosity taken from Ho (2009) unless otherwise specified; the values in this table have been adjusted to account for differences between the adopted distances and those reported in the cited references for the X-ray luminosities. Column (9): Black hole mass derived from the $M_{\rm BH} - \sigma_*$ relation of Greene et al. (2020) unless otherwise specified, with σ_* from Ho et al. (2009). Column (10): Eddington ratios $\lambda_{\rm Edd} = L_{\rm bol}/L_{\rm Edd}$, with $L_{\rm Edd} = 1.26 \times 10^{38}\ (M_{\rm BH}/{\rm M}_\odot)$. [†]: $L_{(2-10){\rm keV}}$ and $M_{\rm BH}$ are taken from Cisternas et al. (2013). [‡]: $L_{(2-10){\rm keV}}$ and $M_{\rm BH}$ are taken from da Silva et al. (2023). [∗]: Inclination angle i, $L_{(2-10){\rm keV}}$, and $M_{\rm BH}$ are taken from Izumi et al. (2018). [⋆]: This target is part of the GATOS sample selected for JWST GO program 4972 but not for new observations, as it was previously observed under GO program 2016.

The analysis presented here is based on JWST MIRI/MRS IFU spectroscopy (Wells et al. 2015; Wright et al. 2023) of the nuclear $r \approx 40 - 240$ pc regions of the five AGN targets, corresponding to the $\sim 4'' \times 4''$ field of view of the observations. The data were acquired through JWST General Observer (GO) programs 2016 (PI: A. Seth; Goold et al. 2026; NGC 4736), 4225 (PI: T. Izumi; the Circinus Galaxy; hereafter Circinus), 4972 (PI: L. Zhang; Zhang et al. 2026; NGC 1097 and NGC 3190), and 7429 (PI: L. Zhang; NGC 7314). All MIRI/MRS observations adopted a 4-point dither with the FASTR1 readout pattern for the source exposures, along with dedicated background exposures obtained using 1-point (non-dither), 2-point dither, or 4-point dither patterns, depending on the program. The total on-source exposure times range from 388 to 1332 seconds, depending on the brightness of each source. The observations of the targets can be accessed via doi: 10.17909/9bgc-da21.

2.2. *Data Processing and Spectral Extraction*

The data were reduced following Zhang et al. (2026), using the JWST Science Calibration Pipeline (v1.18.0; Bushouse et al. 2025), with the context 1364 for the Calibration References Data System. In particular, the `residual_fringe` correction was activated to correct the fringe residuals (Law et al. 2023), and the default `master_bg` function was adopted for background subtraction. In addition, the `firstframe` option was enabled during the data reduction of Circinus to mitigate the saturation effect from this bright source, particularly in Channel 3 (ch3; $\lambda \approx 11.6 - 18.0\,\mu$m). We note that, although this step eliminates saturation effects in the continuum of Circinus, several bright emission lines in ch3, particularly [Ne III]15.56μm, and in a few spaxels, [Ne V]14.32μm, still suffer from saturation near the nucleus. Moreover, H_2 rotational transitions $S(1)$ and $S(2)$ in ch3 are dominated by uncertainties associated with the strong continuum, preventing reliable spaxel-based measurements of these two transitions even in the more extended circumnuclear region of this target. We therefore excluded spaxels in these affected regions from the analysis, except where they were included for illustrative purposes only.

The JWST MIRI/MRS pipeline ultimately produced twelve spectral data cubes across four channels (i.e., ch$1-4$) for each target. Together, these cubes cover the $4.9-27.9\,\mu$m wavelength range with a spectral resolution of $\sim 4000-2000$ (Argyriou et al. 2023; Pontoppidan et al. 2024). A key requirement for spatially resolved analysis is a uniform angular resolution across all slices of the data cubes. Accordingly, we convolved the MRS data cubes from the first three channels (i.e., ch$1-3$; $\lambda \approx 4.9$–$18.0\,\mu$m) to a common point-spread-function (PSF) with a full width at half maximum (FWHM) angular resolution of $0\farcs7$, corresponding to the largest PSF in ch3. The ch4 cubes were retained at their native angular resolution, as the subsequent analysis focuses on emission features covered by the first three channels. Following PSF matching, the spectral data cubes were reprojected onto a common coordinate frame with a pixel size of $0\farcs2$ (i.e., the native pixel size of ch3) prior to spectral extraction. This pixel size corresponds to physical scales of $\sim 4-24$ pc at the distances of the five targets. Spectra extracted from all sub-bands of a given spaxel are stitched together to produce a complete infrared spectrum for each $0\farcs2 \times 0\farcs2$ spaxel, using the ratios of the median fluxes in the overlapping wavelength regions as scaling factors. These factors are generally close to unity, with typical uncertainties of $\sim$10%.

2.3. *Spectral Decomposition and Measurements*

We first decomposed the PAH features using a multi-component fitting approach applied to the extracted spectra of each spaxel (see Appendix A for examples). As detailed by Zhang et al. (2026), the model comprises a series of Drude profiles for individual PAH features, multiple modified blackbodies representing dust components, and a 5000 K blackbody to approximate the stellar continuum, with all emission lines masked during the fitting process. All the model components are subject to foreground screen extinction (i.e., $e^{-\tau_\lambda}$) in the fitting. We adopted here the infrared optical depth curve (i.e., τ_λ) from Smith et al. (2007; their Equation 4), scaled by the fitted free parameter $\tau_{9.7}$, which represents the optical depth at 9.7 μm. The decomposition was performed using the Bayesian Markov Chain Monte Carlo sampler `emcee` in the `Python` environment (Foreman-Mackey et al. 2013), with the median and standard deviation of each parameter's posterior distribution taken as the final estimate and its corresponding uncertainty.

We then fitted H_2 transitions and ionized emission lines in each spaxel individually, using single- and double-Gaussian profiles, respectively, together with a local linear continuum. The fits were optimized via the Levenberg–Marquardt least-squares minimization algorithm. To improve the robustness of the measurements, each emission-line spectrum was perturbed with random noise at the level of its uncertainty, and the fitting was repeated 100 times. The median and standard deviation of these 100 fits were adopted as the final flux and its associated uncertainty for each line. Additionally, all emission-line fluxes were then corrected for dust extinction using the same $e^{-\tau_\lambda}$ curve fitted for each spaxel from the multi-component full-spectrum fitting described above.

3. SPATIALLY RESOLVED ANALYSIS

3.1. *Correlation Between PAH Emission and SF Activity*

Among the molecular, atomic, and ionzied gas phases accessible to JWST spectroscopy, PAH molecules exhibit prominent emission features–particularly around 6.2, 7.7, and 11.3 μm–that are widely calibrated as tracers of star formation rate (SFR; e.g., Treyer et al. 2010; Shipley et al. 2016; Maragkoudakis et al. 2018; Xie & Ho 2019; Zhang & Ho 2023b). However, the intrinsic PAH emission is often relatively suppressed, even deficit, in the harsh environments surrounding AGN (e.g., Smith et al. 2007; O'Dowd et al. 2009; Diamond-Stanic & Rieke 2010; Sales et al. 2010; García-Bernete et al. 2015, 2022a, 2024b; Esparza-Arredondo et al. 2018; Lai et al. 2022; Xie & Ho 2022; Ramos Almeida et al. 2023; Ogle et al. 2025), making it also a diagnostic of AGN feedback (e.g., Zhang et al. 2022, 2024b, 2026 and references therein). In theory, this intrinsic suppression is primarily attributed to the selective erosion and destruction of PAH molecules by the radiative effects of extreme-UV and X-ray photons (Aitken & Roche 1985; Voit 1992), as well as the mechanical processing by shocks (Micelotta et al. 2010a,b).

To compare PAH emission strengths among the five targets at fixed SFRs, we derived spaxel-based SFRs from the infrared neon lines [Ne II]12.81μm, [Ne III]15.56μm, and [Ne V]14.32μm using the AGN-calibrated prescription of Zhuang et al. (2019). This prescription explicitly accounts for the AGN contribution to the neon lines. As shown in Figure 1, spaxels in the central $\sim 4'' \times 4''$ regions of the five AGN lie generally below the unity PAH-SFR relations calibrated by Shipley et al. (2016) for star-forming galaxies.[2] Despite the relative suppression of PAH emission across the sample, spaxels in NGC 4736 and Circinus display relatively enhanced PAH emission at a given SFR compared to those in the other three AGN. This trend does not hold in the inner regions of Circinus, particularly for PAH 11.3 μm feature. As shown in panel (c) of Figure 1 (see also the resolved maps in Section 3.2), this PAH feature exhibits pronounced

[2] The unity relations of Shipley et al. (2016), with the slope fixed at unity, were calibrated using Spitzer/IRS spectroscopy of 105 star-forming galaxies obtained over apertures larger than the pixel scales considered here. Nevertheless, these unity relations provide an appropriate baseline for the qualitative comparisons discussed here. They also derived linear calibrations for the PAH 6.2, 7.7, and 11.3 μm features, with slopes of 1.04, 1.00, and 0.94, respectively.

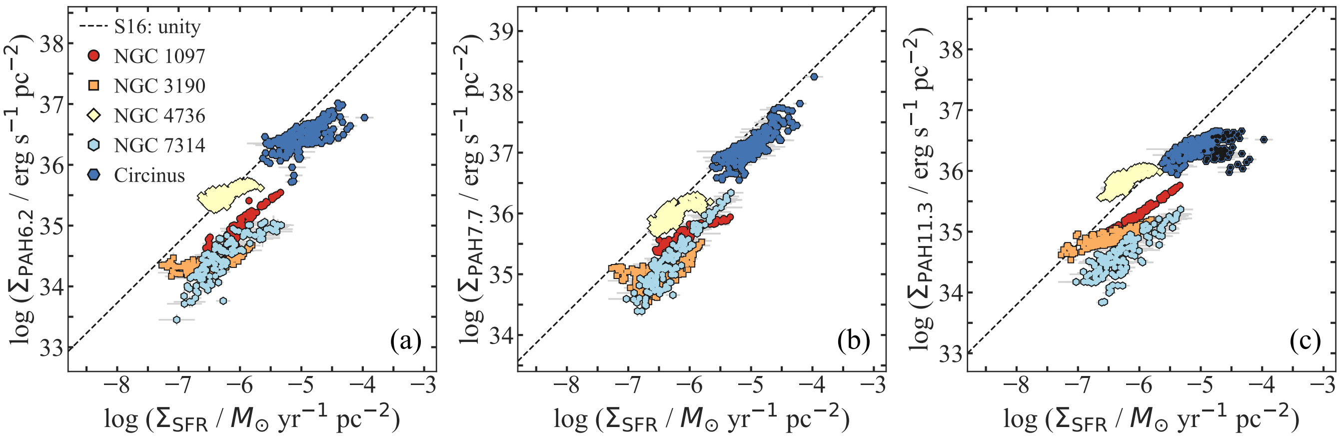

Figure 1. Correlations between the surface brightness of the PAH (a) 6.2 μm (b) 7.7 μm, and (c) 11.3 μm emission and the SFR surface density for $0.''2 \times 0.''2$ spaxels in the central $\sim 4'' \times 4''$ regions of the five AGN targets, where $\Sigma_{\rm PAH} = L_{\rm PAH}\, cos(i)/A$ and $\Sigma_{\rm SFR} = {\rm SFR}\, cos(i)/A$. Here, i is the galaxy inclination angle and A is the spaxel area in ${\rm pc}^2$. The dashed lines represent the unity PAH-SFR relations calibrated by Shipley et al. (2016; S16: unity) for star-forming galaxies. The data points highlighted with black dots represent spaxels in the central $r \approx 15 - 25$ pc region of Circinus (the inner region is excluded from the analysis, as detailed in Section 2.2). Unless otherwise specified, the analysis presented here and in subsequent figures includes only spaxels with measurements of all five H_2 transitions required for the shock-processing indicator and all three neon emission lines used for SFR estimation and the AGN-irradiation indicator.

suppression in the inner regions of Circinus, reaching levels comparable to those observed in NGC 7314. Such increasing suppression of PAH 11.3 μm feature toward the Circinus nucleus has also been reported by Jensen et al. (2017; see Figure 2 therein). The relatively stronger PAH emission in spaxels in NGC 4736 and Circinus outer-circumnuclear regions compared to the other three AGN is likely attributable to the (post-)starburst nature (Pellegrini et al. 2002; Marconi et al. 1994) of their central regions. In contrast, the relative suppression of PAH 11.3 μm feature in NGC 7314 and the inner regions of Circinus compared to the other three AGN reflects a reduced abundance of neutral PAHs, likely caused by the preferential ionization of PAHs in these environments, as discussed with model results in Section 3.2.

As noted above, the relative suppression of intrinsic PAH emission in the vicinity of AGN is in theory attributed to the selective erosion and destruction of PAHs, primarily driven by AGN irradiation and shock processing that represent distinct modes of AGN feedback. Following this point, we performed a multiple linear regression analysis with the `Python` package `statsmodels` (Seabold & Perktold 2010). This analysis aims to reproduce the observed PAH surface brightness (in unit of ${\rm erg\,s^{-1}\,pc^{-2}}$) as a function of SFR surface density (in unit of ${\rm M_\odot\,pc^{-2}}$), the ratio of the summed H_2 $S(1)$ – $S(5)$ emission to PAH 7.7 μm feature (i.e., H_2 $S(1$–$5)$/PAH7.7; hereafter $\rm rH_2$), and the ratio of [Ne V]14.32μm emission to PAH 11.3 μm feature (i.e., [Ne V]14.32/PAH11.3; hereafter rNe). The ratio of infrared H_2 transitions to PAH emission has long been proposed as a powerful tracer of shocks, as the intensities of infrared H_2 transitions generally scale closely with PAH emission over a wide range of radiation field strengths, whereas shock heating can produce an excess of H_2 emission (e.g., Roussel et al. 2007; Ogle et al. 2010; Guillard et al. 2012; Riffel et al. 2020; Kristensen et al. 2023). We adopt the ratio of the high-ionization [Ne V] line to PAH emission as an indicator of AGN irradiation strength because the strength of this coronal line has been shown to correlate strongly with AGN luminosity over a wide range of luminosities and physical conditions. (e.g., Weaver et al. 2010; García-Bernete et al. 2017; Bierschenk et al. 2024; Annuar et al. 2025; Goold et al. 2026). We note that the diagram consisting of these two ratios efficiently distinguish the two Seyfert galaxies from the three LINERs studied here (see Figure A1 in Appendix A).

The multiple linear regression analysis yields

$$\log \Sigma_{\rm PAH}^{\rm fit} = \alpha_1 \log \Sigma_{\rm SFR} + \alpha_2 \log {\rm rH_2} + \alpha_3 \log {\rm rNe} + \beta, \tag{1}$$

where the coefficients α_1, α_2, α_3, and β for PAH 6.2, 7.7, and 11.3 μm features are listed in Table A1 in Appendix A. As shown in Figure 2, the multiple linear regression model incorporating SFR, $\rm rH_2$, and rNe reproduces the observed PAH emission well, with root-mean-square (RMS) scatters (σ in Table A1) of 0.25, 0.19, and 0.21 dex for PAH 6.2, 7.7, and 11.3 μm features, respectively. These tight correlations support the interpretation that the general suppression of PAH emission in AGN, relative to that expected at a given SFR, is governed by the combined effects of AGN irradiation and shock processing.

Intriguingly, the fitted correlation for PAH 7.7 μm feature exhibits the smallest scatter among the three PAH features, suggesting that it provides the most robust tracer of SFR in

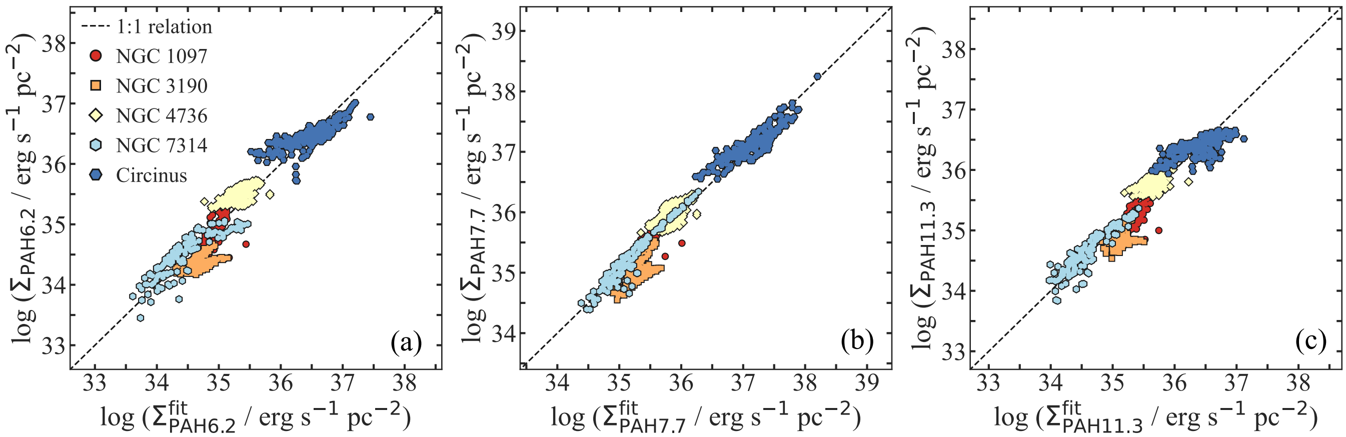

Figure 2. Correlations between the surface brightness of the measured PAH (a) 6.2 μm, (b) 7.7 μm, and (c) 11.3 μm emission and those predicted by Equation 1 for data points in Figure 1, with the dashed line in each panel indicating the 1:1 relation.

the targets studied here. This result is noteworthy given the lack of consensus among previous studies on which PAH feature serves as the best SFR indicator, with some studies reporting consistent results and others reaching conflicting conclusions. Specifically, Diamond-Stanic & Rieke (2010), based on an analysis of 35 Seyfert nuclei on sub-kpc scales, argued that PAH 11.3 μm feature, unlike PAH 7.7 μm feature, remains a robust tracer of SFR–as indicated by the [Ne II]12.81μm emission–even in nuclei exhibiting unusually high PAH 11.3/7.7 ratios. In contrast, LaMassa et al. (2012), analyzing a larger sample of 264 star-forming galaxies, 51 composites, and 73 AGN over kpc scales, found that PAH 11.3 μm feature is significantly suppressed relative to PAH 7.7 μm feature in most of their AGN, raising concerns about its reliability as a standalone SFR indicator in such environments. Later, Esquej et al. (2014) analyzed the equivalent width of PAH 11.3 μm feature (hereafter PAH EW11.3) in a sample of 29 Seyfert nuclei on sub-100-pc scales and found no significant dependence of PAH EW11.3 on AGN luminosity. They therefore concluded that there is no general evidence for suppression of PAH 11.3 μm feature in the vicinity of AGN, supporting its use as an SFR proxy. Nevertheless, they also reported that PAH 11.3 μm feature is undetected in the central $\sim$15 pc region of Circinus, corroborating the earlier findings of Roche et al. (2006) and consistent with the trend of increasing suppression of this feature in Circinus nucleus found here. Our results are broadly consistent with the conclusions of LaMassa et al. (2012). Additional support comes from the linear PAH–SFR calibrations of Shipley et al. (2016), which give a linear relation (slope = 1.0) for PAH 7.7 μm feature but a slightly sublinear relation (slope = 0.94) for PAH 11.3 μm feature. In Section 4, we explore the physical mechanisms responsible for these disparate results and show that they can be explained by differences in sample selection within a unified framework that accounts for the combined effects of AGN irradiation and shock processing.

We additionally performed a complementary multiple linear regression analysis to calibrate the SFR surface density (in unit of $\mathrm{M_\odot\,pc^{-2}}$) as a function of PAH surface brightness (in unit of $\mathrm{erg\,s^{-1}\,pc^{-2}}$), $\mathrm{rH_2}$, and rNe, thereby demonstrating the practical application of the above results for deriving SFRs from PAH emission in AGN. The complementary multiple linear regression analysis yields

$$\log \Sigma_{\rm SFR} = \alpha_1 \log \Sigma_{\rm PAH} + \alpha_2 \log {\rm rH_2} + \alpha_3 \log {\rm rNe} + \beta \quad (2)$$

where the coefficients α_1, α_2, α_3, and β for PAH 6.2, 7.7, and 11.3 μm features are listed in Table A2 in Appendix A. This multiple linear regression model yields PAH-based SFRs that are well correlated with the neon-based SFR, with RMS scatters of 0.24, 0.20, and 0.24 dex for PAH 6.2, 7.7, and 11.3 μm features, respectively. By explicitly incorporating the effects of AGN irradiation and shock processing on PAH emission, this multiple linear regression approach offers a new method for calibrating SFR in AGN, warranting validation and refinement with larger samples in future studies.

3.2. *Correlation Between PAH Emission and AGN Activity*

Beyond the intrinsic strength of individual PAH features, the observed ratios among different PAH features encode rich information about the size distribution and ionization state of PAH molecules, as well as the radiation field in which they are embedded (e.g., Draine & Li 2007; Draine et al. 2021; Rigopoulou et al. 2021, 2024, and for reviews see Tielens 2008; Li 2020). In short, smaller PAHs emit more strongly at shorter (i.e., more energetic) wavelengths, as their lower heat capacity leads to higher excitation levels following the absorption of a UV photon. Neutral PAHs exhibit stronger 3.3 and 11.3 μm features due to more prominent C–H vibrational modes, whereas ionized (cationic) PAHs preferentially emit in the 6–9 μm range, where C–C vibrational modes dominate. Furthermore, a moderately stronger radiation field in-

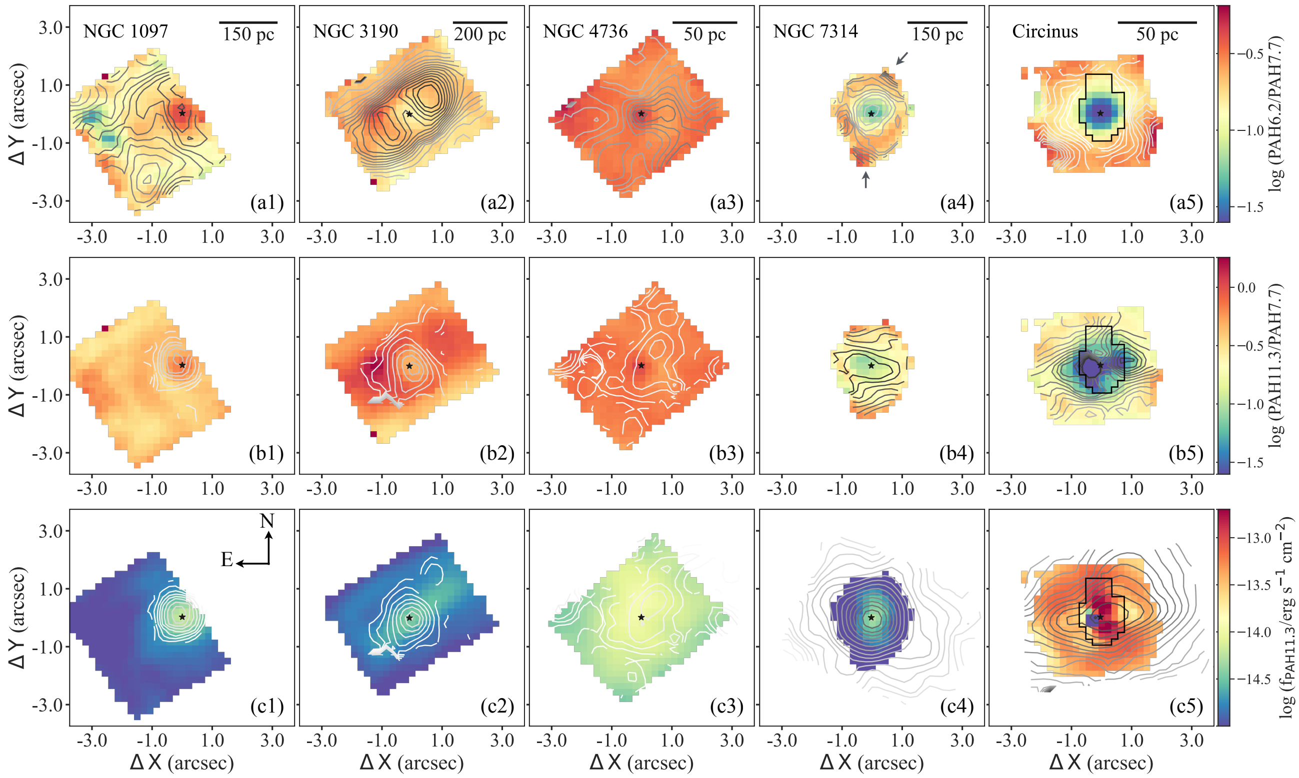

Figure 3. Spatially resolved maps of PAH 6.2/7.7 ratio (top panels), PAH 11.3/7.7 ratio (middle panels), and PAH 11.3 μm emission (bottom panels) for the five AGN targets. Each column corresponds to one target, with the AGN position denoted by a black star. A common color scale is adopted for all panels within a given row and is shown on the right. The contours in the top, middle, and bottom panels show the distributions of $\log(\mathrm{rH_2})$ (-2.25 to -0.5), $\log(\mathrm{rNe})$ (-4.0 to 0.15), and $\log(f_{\mathrm{[Ne\ V]14.32\mu m}}/\mathrm{erg\,s^{-1}\,cm^{-2}})$ (-18.0 to -13.3), respectively, with higher values indicated by darker colors on a common scale for each row. The black arrows in panel (a4) indicate the locations of the two radio spots in NGC 7314. The black polygons in Circinus outline the region within which the spaxels are shown here for illustrative purposes; these spaxels are excluded from the statistical analyses due to the lack of reliable spaxel-based measurements of [Ne III]15.56μm and/or H_2 $S(1)$ and $S(2)$, as detailed in Section 2.2. North is up in all panels, and the physical scale of each target is labeled in the top-right corner of each top panel.

creases the PAH ionization fraction, and a harder, FUV-rich radiation field enhances the relative strength of the shorter-wavelength PAH features prior to their photo-destruction. In other words, variations in the observed PAH band ratios reflect changes in the underlying physical conditions, including those driven by different modes of AGN feedback.

As presented in Figure 3, the spatially resolved maps of the two most widely used PAH 6.2/7.7 (top panels) and 11.3/7.7 (middle panels) ratios exhibit pronounced spatial variations, reflecting modifications in PAH properties toward the nucleus of each target. In particular, the nuclei of the two Seyfert galaxies studied here show systematically lower PAH 6.2/7.7 and 11.3/7.7 ratios (< 0.3 and < 0.35, respectively, at $r < 1''$) than the three LINERs studied here. These lower ratios are plausibly driven by strong AGN irradiation, as indicated by the darker contours in panels (b4) and (b5) of Figure 3, which trace regions of elevated rNe values. In contrast, the comparatively higher PAH 11.3/7.7 ratios observed in the three LINERs are more likely associated with shock processing, as suggested by the darker contours in panels (a1)$-$(a3) of Figure 3, which trace regions of elevated $\mathrm{rH_2}$ values (see also Zhang et al. 2026 for a detailed discussion of the role of shock processing in these LINERs). As discussed below and further elaborated in Section 4, this difference is not merely a consequence of AGN type, but instead reflects the distinct physical conditions driven by different modes of AGN feedback. We also note that, although NGC 3190 exhibits overall large PAH 6.2/7.7 and 11.3/7.7 ratios, its nucleus shows a modest decrease in these ratios. This behavior is likely driven by the combined effects of the spatially concentrated AGN-irradiation-dominated region and relatively weak shock processing around the nucleus, as evidenced by the nuclear rNe peak and $\mathrm{rH_2}$ valley in panels (b2) and (a2) of Figure 3.

Other noteworthy features in Figure 3 include compact structures in NGC 1097 that exhibit lower PAH 6.2/7.7 ratios toward the east (see the greenish regions in panel a1). These structures are also evident in low-ionization emission line maps (e.g., [Ar II]6.98μm, [Ne II]12.81μm), but are absent in higher-ionization (e.g., [Ne III]15.56μm, [O IV]25.89μm) and H_2 emission line maps not shown here. In NGC 7314,

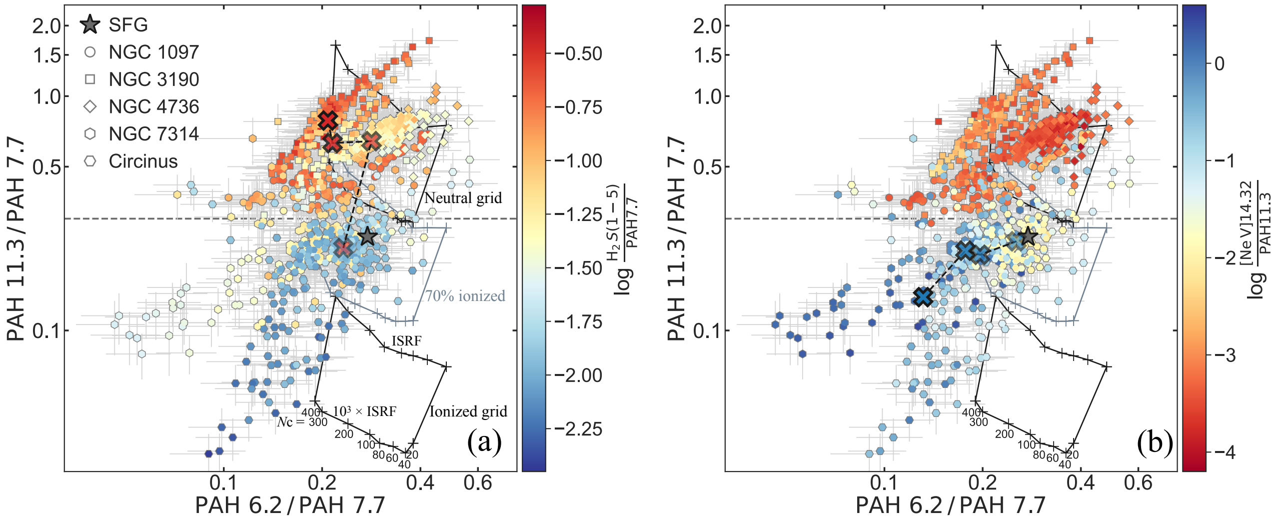

Figure 4. PAH band ratio diagrams for $0''.2 \times 0''.2$ spaxels in the central $\sim 4'' \times 4''$ regions of the five AGN targets, color-coded by the strength indicators of (a) shock processing ($\mathrm{rH_2}$) and (b) AGN irradiation (rNe), respectively. The horizontal dashed lines mark the empirical demarcation at PAH 11.3/7.7 = 0.3. The reddish and bluish crosses in panels (a) and (b) show, for the five AGN targets, the median PAH band ratios of the spaxels in bins of increasing $\log(\mathrm{rH_2})$ of $[-2, -1.5]$, $[-1.5, -1.0]$, $[-1.0, -0.5]$, and $[-0.5, 0]$, and increasing $\log(\mathrm{rNe})$ of $[-2, -1.5]$, $[-1.5, -0.75]$, $[-0.75, 0]$, and $[0, 0.5]$ (from light to dark), respectively. The gray star labeled "SFG" represents the median PAH band ratios of the spatially resolved spaxels in star-forming galaxies measured by Zhang et al. (2022); the individual SF spaxels, which are clustered around the median value, are omitted for clarity. The grids marked by '+' in each panel show model predictions of PAH band ratios from Rigopoulou et al. (2024) for neutral (top grids), 70% ionized (middle grids), and fully ionized (bottom grids) PAHs of various sizes (carbon number $N_{\mathrm{C}} = 20 - 400$, increasing from the right to the left boundary of each grid). The grids span the interstellar radiation field (ISRF; top boundary) up to $10^3 \times$ISRF (bottom boundary).

the two regions at the northern and southern tips that show modestly enhanced shock processing, i.e., higher $\mathrm{rH_2}$ values as shown in panel (a4), are spatially associated with two radio spots detected by Thean et al. (2000). Additionally, the tilted east-west elongated regions exhibiting strong AGN irradiation, i.e., higher rNe values as shown in panel (b4), align with the orientation of its AGN ionization cone, which has a wide opening angle as revealed by high-ionization emission-line maps (see e.g., panel c4 and also da Silva et al. 2023). In contrast, the modest north-south elongation of the circumnuclear PAH emission in NGC 7314 (see panel c4) is spatially coincident with the circumnuclear cold gas distribution and aligned with the inner dusty molecular torus (García-Burillo et al. 2021). In Circinus, the regions with low PAH 11.3/7.7 ratios also coincide with the ionization cone traced by high-ionization emission-line maps (see e.g., panel c5 and also Marconi et al. 1994), as well as the polar dust elongation (Izumi et al. 2018; Lopez-Rodriguez et al. 2026); however, note that the PAH measurements may be biased by the strong continuum of this target in the circumnuclear region outlined by the black polygons in the rightmost panels. These spaxels were therefore excluded from all statistical analyses presented in this study.

In the following, we focus on the physical insights provided by the PAH band ratios of the spaxels in the five AGN, in combination with the diagnostic ratios $\mathrm{rH_2}$ and rNe. As shown in Figure 4, the spaxels in the five AGN overall exhibit lower PAH 6.2/7.7 ratios compared to the spaxels in star-forming galaxies. More importantly, the spaxels in the targets studied here exhibit a bimodal distribution of PAH 11.3/7.7 ratios (with PAH 11.3/7.7 = 0.3 serving as a useful demarcation), as already seen in their spatially resolved maps. Relative to spaxels in star-forming galaxies, the spaxels in the LINERs and Seyfert galaxies studied here display systematically higher and lower PAH 11.3/7.7 ratios, respectively. As indicated by the color coding, this bimodal distribution appears to arise from the combined influence of enhanced shock processing in the three LINERs and stronger AGN irradiation in the two Seyfert galaxies, with star formation activity providing the underlying baseline. As outlined in Section 3.1 and discussed further below, the lower PAH 11.3/7.7 ratios in the two Seyferts are primarily driven by the relative suppression of their PAH 11.3 μm emission, reflecting a lower fraction of neutral PAHs. To highlight these trends, we plot for the five AGN the median PAH band ratios of the spaxels in bins of increasing $\log(\mathrm{rH_2})$ and $\log(\mathrm{rNe})$ as reddish and bluish crosses (from light to dark) in panels (a) and (b) of Figures 4, respectively. These reddish and bluish crosses clearly trace two distinct trends of progressively stronger PAH modifications associated with enhanced shock processing and stronger AGN irradiation, respectively. Note again that this difference is not merely a consequence

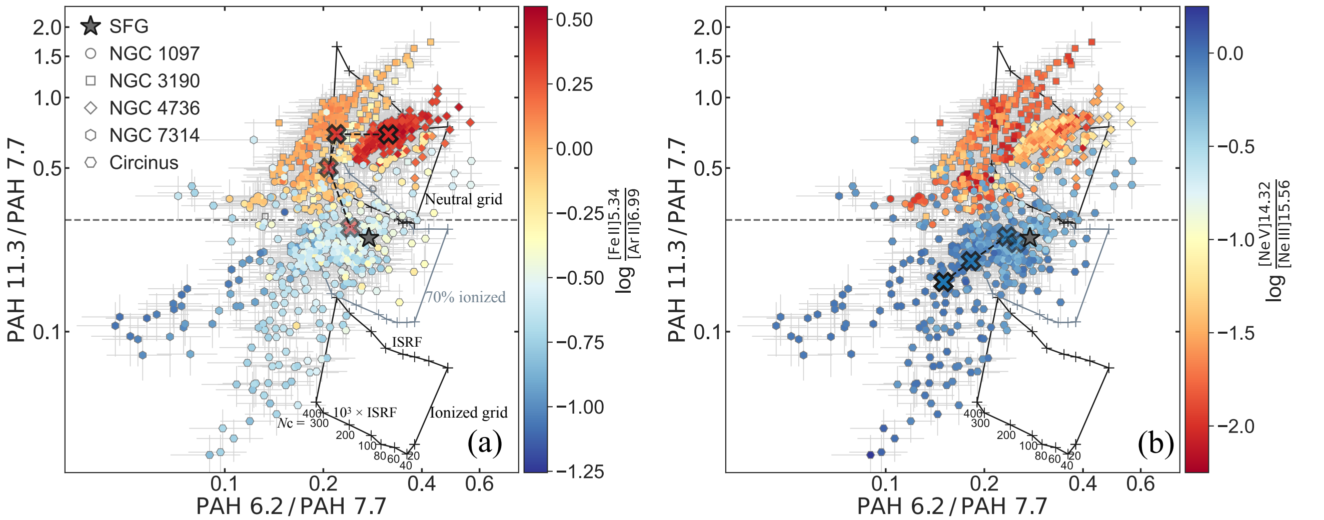

Figure 5. Same as Figure 4 but color-coded by the different strength indicators of (a) shock processing ([Fe II]5.34/[Ar II]6.99) and (b) AGN irradiation ([Ne V]14.32/[Ne III]15.56). The reddish and bluish crosses in panels (a) and (b) show, for the five AGN targets, the median PAH band ratios of the spaxels in bins of increasing log ([Fe II]5.34/[Ar II]6.99) of $[-0.5, -0.25]$, $[-0.25, 0]$, $[0, 0.25]$, and $[0.25, 0.5]$, and increasing log ([Ne V]14.32/[Ne III]15.56) of $[-0.5, -0.3]$, $[-0.3, -0.15]$, $[-0.15, 0]$, and $[0, 0.2]$ (from light to dark), respectively.

of AGN type, but instead reflects the distinct physical conditions associated with the two modes of AGN feedback.

The model grids in Figure 4 confirm that the systematically higher and lower PAH 11.3/7.7 ratios observed in the three LINERs and the two Seyfert galaxies, respectively, correspond to larger fractions of neutral and ionized PAHs, while the generally lower PAH 6.2/7.7 ratios indicate relatively larger PAH sizes. As discussed by Zhang et al. (2026), a natural explanation for this bimodal distribution is that shock processing, if present, preferentially destroy both smaller and more vulnerable ionized PAHs (Allain et al. 1996; Holm et al. 2011), leading to a relative enhancement of larger, neutral PAHs. In contrast, intense AGN irradiation, as observed in the two Seyfert galaxies studied here, preferentially ionizes PAHs and subsequently destroys most of the smaller grains, resulting in a relative enhancement of larger, ionized PAHs. In particular, for spaxels in NGC 7314, which exhibits both strong AGN irradiation and moderate shock processing, the bimodal distribution in their PAH band ratios is most consistent with this scenario, as further elaborated in Section 4. Direct destruction of PAHs by hard X-ray photons, without prior ionization, may mimic the effects of shock processing (Micelotta et al. 2010b), highlighting the need for dedicated studies of X-ray-rich environments around more luminous AGN. Partially destroyed PAHs with open or irregular structures and increased hydrogenation (e.g., catacondensed PAHs) may exhibit enhanced PAH 11.3/7.7 ratios (e.g., Pantoni et al. 2026; Li 2020), although this interpretation remains debated (Rigopoulou et al. 2024).

To further confirm the two distinct trends of progressive PAH modifications, we turn to additional independent diagnostics based on infrared ionized emission lines. Here, we use the [Ne V]14.32/[Ne III]15.56 ratio as an additional proxy for AGN irradiation, as it is less susceptible to star formation activity and correlates well with the ionization parameter U in AGN (Zhang et al. 2025). In addition, we adopt the [Fe II]5.34/[Ar II]6.99 ratio as a proxy for shock processing, which is sensitive to shocks because fast shocks can efficiently liberate iron from dust grains while having little effect on the noble gas argon. Previous studies have shown that enhanced [Fe II] emission in AGN is closely associated with shocked regions (e.g., Forbes & Ward 1993; Mouri et al. 2000; Storchi-Bergmann et al. 2009; Colina et al. 2015; Koo et al. 2016; Rodríguez-Ardila et al. 2017; Durré & Mould 2018; Riffel et al. 2021; Costa-Souza et al. 2026). The diagrams consisting of these ionized emission-line ratios efficiently distinguish the two Seyfert galaxies from the three LINERs (see Figure A2 in Appendix A): the former are dominated by AGN excitation, whereas the latter are better explained by shock excitation. Correspondingly, we revisit Figure 4, but now color-code the data points using these ionized emission-line ratio diagnostics. As shown in Figure 5, the two distinct trends of progressive PAH modifications remain evident, although some discrepancies between Figures 4 and 5 are also present, particularly in panel (a).

In contrast to Figure 4(a), Figure 5(a) exhibits a different final direction of the red crosses, driven by the highly elevated [Fe II]5.34/[Ar II]6.99 ratios in NGC 4736. A similar elevation is plausibly also present in Circinus, with NGC 7314 serving as a reference. This result is not surprising, as the shocks that enhance H_2 emission are not necessarily the same as those responsible for enhancing [Fe II] emission (e.g., Hollenbach & McKee 1989; Mouri et al. 2000; Allen et al. 2008; Kristensen et al. 2023); in particular, the fast shocks (with velocities of hundreds of $\mathrm{km\,s^{-1}}$) required to produce ionized gas emission would instead lead to H_2 dissociation. As discussed by Riffel et al. (2026a), H_2 emission is more likely to originate in post-shock gas, where molecules reform after being dissociated by the fast shocks responsible for ionized gas emission (e.g., Guillard et al. 2009; Richings & Faucher-Giguère 2018a,b). Again, the difference between Figures 4(a) and 5(a) is likely related to the (post-)starburst nature of the central regions in NGC 4736 and Circinus, given that both X-ray irradiation and shock heating can contribute to [Fe II] emission (e.g., Mouri et al. 2000; Allen et al. 2008; Dors et al. 2012). Specifically, a cluster of at least four bright point-like X-ray sources is present in the central $r \leq 5''$ region of NGC 4736, with the brightest ones attributed to gas heated by supernovae rather than the low-luminosity AGN at its center (see Pellegrini et al. 2002). Despite the differences, Figures 4 and 5 consistently support the existence of two distinct AGN feedback modes: one associated with shock processing and the other with AGN irradiation, although supernovae in (post-)starburst environments may also contribute to shock processing and the resulting PAH modifications.

In summary, regardless of the diagnostics employed, the spaxels in the five AGN consistently reveal two clearly distinguishable trends of progressive PAH modification associated with the two AGN feedback modes. We also confirm that the bimodal distribution and the two distinct trends discussed above persist when the y-axis is replaced by the PAH 11.3/6.2 ratio (see Figure A3 in Appendix A), which also traces PAH ionization and is less sensitive to continuum contamination. In addition, the PAH band ratios derived from integrated spectra extracted within large apertures, $r \leq 0''.5$, $0''.5 \leq r \leq 1''.0$, and $1''.0 \leq r \leq 1''.5$, exhibit the the same bimodal distribution as those observed among the spaxels in the five AGN (see the black-outlined points in Figure A3), demonstrating that these trends are robust against potential PSF-related artifacts. This result is expected, as all spectral data cubes were convolved to a common PSF prior to the spaxel-based measurements. Also note that all targets studied here exhibit prominent PAH features in the JWST/MRS spectra (see Figure A4 and Table A3 in Appendix A for examples); therefore, the two distinct trends are unlikely to arise from noise-induced artifacts. In short, the two distinct trends observed among the spaxels across the five targets naturally reflect the two primary modes of AGN feedback, as illustrated in Figure 6 and discussed in detail in Section 4.

Additionally, we note that different analysis methods (e.g., `PAHFIT`, Smith et al. 2007; `CAFE`, Marshall et al. 2007; `SPIRIT`, Donnan et al. 2024; `PAHdb`, Maragkoudakis et al. 2025) can yield systematically different PAH measurements from JWST spectra. The resulting differences in derived PAH fluxes between `CAFE` and `SPIRIT` can commonly reach a factor of $\sim$2, with `SPIRIT` generally yielding lower PAH fluxes (Pantoni et al. 2026). In addition, decompositions based on `PAHFIT` and `CAFE` differ from `PAHdb` modeling by $\sim$7% in the inferred PAH ionization fraction (Maragkoudakis et al. 2025). Specifically, for spectra extracted from the $r = 0''.5 - 1''.0$ apertures in the five targets, `SPIRIT` yields PAH 6.2/7.7 and 11.3/7.7 ratios that are systematically more than $\sim$20% higher, respectively, than those derived using the method adopted in this work (which is essentially equivalent to `PAHFIT`), with differences exceeding 100% in some cases. The differences in the measurements primarily arise from the different treatments of extinction and dust continuum, which consequently lead to systematic differences in the derived PAH measurements (see also discussion in Van De Putte et al. 2025). We therefore caution readers that systematic differences among analysis methods may lead to different interpretations of the observations. Nevertheless, the two distinct trends of progressive PAH modification observed across the five targets presented here are consistently supported by multiple diagnostics presented above, together with the additional evidence discussed in Section 4. This consistency strongly suggests that these trends are robust and reflect genuine physical differences rather than methodological artifacts.

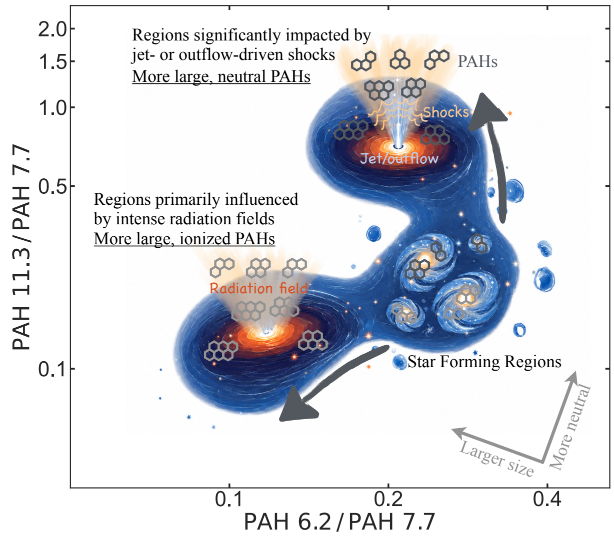

Figure 6. Illustrative schematic showing the two regimes in our AGN targets affected by the two feedback modes associated with AGN irradiation and shock processing, respectively. Gray arrows in the lower right corner indicate the directions in theory of increasing overall PAH size and neutral fraction as the PAH band ratios change. Using star-forming regions as a baseline, AGN irradiation tends to drive the heating and ionization of PAH molecules, followed by the preferential photodestruction of smaller PAHs, leading to a population dominated by larger and more ionized PAHs. In contrast, shock processing appears to preferentially destroy ionized PAHs, resulting in a higher survival fraction of large and neutral PAHs.

4. IMPLICATIONS FOR AGN FEEDBACK MODES

4.1. *Coexistence of Kinetic and Radiative AGN Feedback*

As reported by Zhang et al. (2026), the H_2 transitions in the nuclear regions of the three LINERs studied here are not fully thermalized, with slow, plausibly jet-driven molecular shocks associated with AGN providing the additional excitation. Specifically, matching the observed H_2 line ratios, $S(3)/S(1)$ and 1-0 $O(5)/S(3)$, to the predictions of the theoretical models of Kristensen et al. (2023) indicates the presence of C-type molecular shocks with velocities of $v_{\rm s} \lesssim 10\,{\rm km\,s^{-1}}$. Moreover, they found that coupling only $\sim 0.1-1\%$ of the AGN jet power to the surrounding gas is sufficient to reproduce the observed H_2 fluxes in the nuclear regions of the three LINERs. Consistently, growing evidence suggests that the central engines of low-luminosity AGN are often dominated by jet power (e.g., Fernández-Ontiveros et al. 2012; Goold et al. 2026), producing radio jets that span pc to kpc scales, depending on the jet power (Mezcua & Prieto 2014). In contrast, Figure A2 shows that the radiative shocks traced by ionized emission lines have much higher velocities, with $v_{\rm s} \approx 100-400\,{\rm km\,s^{-1}}$, consistent with the shock velocity range of $\sim 200-300\,{\rm km\,s^{-1}}$ modeled by Dopita et al. (2015) for the prototypical LINER NGC 1052. As discussed by Goold et al. (2024), the fast radiative shocks observed in the low-luminosity AGN are likely driven by outflows powered by radiatively inefficient accretion flows (RIAFs) or by radio jets. The distinct shock velocities traced by the H_2 transitions and ionized emission lines in the three LINERs are consistent with the broader line widths and blueshifted ionized emission-line profiles observed in their nuclear regions (Zhang et al. 2026).

PAH emission primarily arises from photodissociation regions adjacent to warm molecular gas (e.g., Chown et al. 2025; Maragkoudakis et al. 2026) and is well correlated with the cold molecular gas component (e.g., Cortzen et al. 2019; Leroy et al. 2023; Zhang & Ho 2023a). In addition, even large PAHs with $N_{\rm C} = 200$ are expected to be destroyed by shocks with $v_{\rm s} \geq 125\,{\rm km\,s^{-1}}$ (Micelotta et al. 2010a). Given the tight correlation between PAH emission and the cold gas component, as well as the survival of PAHs with $N_{\rm C} \leq 200$ in regions dominated by shock processing across the five targets (Figures 4 and 5), the observed shock processing of PAHs is likely dominated by low-velocity molecular shocks, while high-velocity radiative shocks may also play a significant role. Conservatively, the shocks responsible for modifying PAH properties are not necessarily limited to velocities of $\lesssim 10\,{\rm km\,s^{-1}}$ but are likely to have velocities below $100\,{\rm km\,s^{-1}}$. Additional evidence for the importance of low-velocity shocks comes from the temperature distributions of warm molecular gas. Under local thermodynamic equilibrium, the relative populations of H_2 pure rotational transitions can be described by a power-law temperature distribution, $dN = mT^{-\beta}dT$, where lower values of β indicate a larger fraction of warmer molecular gas and thus stronger heating by the underlying feedback processes. Following the methodology of Togi & Smith (2016), we derived β values across the fields of view of the five targets by fitting the six H_2 pure rotational transitions, $S(1)-S(6)$. We find that shock-dominated regions exhibit $\beta \gtrsim 4.6$, whereas irradiation-dominated regions have $\beta \lesssim 4.6$, with the latter consistent with the range commonly observed in Seyfert nuclei (e.g., Zhang & Ho 2023c; Davies et al. 2024; Delaney et al. 2026). The larger β values in shock-dominated regions are consistent with low-velocity shocks that primarily heat the lower-excitation H_2 rotational levels. In contrast, sufficiently strong shocks, same as AGN irradiation, can populate higher-J H_2 rotational levels, producing flatter temperature distributions and consequently lower β values.

As shown in Figure 3, the spaxels in the innermost region of NGC 7314 exhibit PAH band ratios indicative of a relatively high abundance of large PAHs and a high, though not extreme, ionization fraction. These results likely reflect the combined effects of the intense AGN irradiation in this target, which tends to ionize all and destroy smaller PAHs, together with modest shock processing, which preferentially enhances the destruction of fully ionized PAHs. The presence of notably large and ionized PAHs in the nuclear region of NGC 7314 is also reported by Diamond-Stanic & Rieke (2010; see Figure 8 therein). Their measurements of PAH 6.2/7.7 ≈ 0.14 and 11.3/7.7 ≈ 0.21 from Spitzer/IRS spectroscopy place NGC 7314 at the extreme left of their PAH 11.3/7.7 vs PAH 6.2/7.7 diagram, distinguishing it from the nuclei of other Seyfert galaxies in their sample. More intriguingly, in the nuclear region of NGC 7314 examined here, larger and more highly ionized PAHs preferentially trace the AGN ionization cone (Section 3.2), whereas larger but weakly ionized, and even neutral, PAHs are predominantly found along its periphery, particularly in regions spatially associated with the two radio spots that exhibit evidence of enhanced shock processing. Specifically, spaxels in NGC 7314 with PAH 11.3/7.7 > 0.4 (predominantly neutral PAHs) exhibit $\log({\rm rH_2})$ and $\log({\rm rNe})$ values of ~ -1.15 to -0.65 and ~ -1.05 to -0.40, respectively (see Figure A1). By contrast, spaxels in NGC 7314 with PAH 11.3/7.7 < 0.2 and 6.2/7.7 < 0.15 (predominantly ionized PAHs) show values that fall below and above these ranges, respectively, namely ~ -1.60 to -1.30 (relatively weaker shock processing) and ~ -0.10 to 0.45 (relatively stronger AGN irradiation). This trend is qualitatively the same for the diagnostics based solely on ionized-emission lines (see Figure A2). Notably, all the spaxels in NGC 7314 with PAH 11.3/7.7 > 0.4 have $\log({\rm rH_2})$ values above the threshold for a significant shock contribution (i.e., -1.45; Guillard et al. 2012; Zhang et al. 2026), highlighting the importance of shock processing in shaping PAH properties even in Seyfert galaxies.

Furthermore, according to García-Bernete et al. (2024b), JWST spectroscopy shows that the arcsecond-scale nuclear regions of three Seyfert galaxies with $\log L_{\rm bol}/{\rm erg\,s^{-1}} \approx 44.2-44.3$, as well as their off-nuclear regions along the projected directions of AGN-driven outflows, exhibit elevated PAH 11.3/7.7 ratios and reduced PAH 6.2/7.7 ratios. Their PAH measurements (PAH 11.3/7.7 ~ 0.5 and PAH 6.2/7.7 $\sim 0.1-0.4$) in these regions are consistent with the values of the NGC 7314 spaxels located at the periphery of the AGN ionization cone, particularly those in regions exhibiting stronger shock processing. Importantly, García-Bernete et al. (2024b) also reported elevated H_2/PAH ratios in the nuclear regions of these Seyfert galaxies and along their projected outflow directions, which coincide with their radio jet axes (Zhang et al. 2024a). More quantitatively, Zhang et al. (2024b) showed with JWST spectroscopy of another three Seyfert galaxies ($\log L_{\rm bol}/{\rm erg\,s^{-1}} \approx 43.4-44.3$) that the $3'' \times 3''$ apertures with PAH 11.3/7.7 > 0.4 exhibit $\log({\rm rH_2})$ values of ~ -1.00 to -0.05, comparable to those observed in the three LINERs discussed here (see Figure 6 in Zhang et al. 2026). In contrast, the central $3'' \times 3''$ aperture of MCG-05-23-016 (PAH 11.3/7.7 $= 0.37$), the only one among the three Seyfert galaxies where radiative effects play an important role as discussed therein, exhibits a comparatively lower $\log({\rm rH_2})$ value of -1.27 ± 0.18. In addition, according to Zhang & Ho (2023c), JWST spectroscopy shows that most 100-pc-scale spaxels in the circumnuclear region of NGC 7469 ($\log L_{\rm bol}/{\rm erg\,s^{-1}} \approx 44.5$) exhibit PAH band ratios consistent with star-forming regions, particularly those located on the nuclear starburst ring; however, the innermost spaxels in NGC 7469 show elevated PAH 11.3/7.7 ratios of $\sim 0.4-0.5$, along with signatures of outflows. In particular, spaxels in the innermost 200 pc of NGC 7469 exhibit $\log({\rm rH_2})$ and $\log({\rm rNe})$ values of -1.35 and -0.80, respectively, consistent with a substantial shock contribution and comparatively weak AGN irradiation. These results further suggest that shock processing plays an important role in shaping the observed PAH properties even in Seyfert galaxies. However, we caution that direct destruction of PAHs by X-ray photons may also contribute in these higher-luminosity Seyfert nuclei, as noted in Section 3.2.

4.2. *A Practical Unified Framework for AGN Feedback*

Considered together, the JWST measurements in the literature and the spatially resolved results presented here suggest that, when AGN irradiation is the dominant feedback mechanism, it primarily modifies PAHs through radiative heating and ionization while preferentially photo-destroying the smaller PAHs. In the five targets examined here, this mode of feedback appears to be largely associated with AGN ionization cones. This scenario is consistent with the findings of Xie & Ho (2022), who reported elevated fractions of large and ionized PAHs on global scale (i.e., ~ 10 kpc) in a sample of 86 low-redshift ($z \approx 0.05-0.4$) quasars with $\log L_{\rm bol}/{\rm erg\,s^{-1}} \geq 44.5$, a regime in which radiative-mode feedback is expected to dominate globally. In contrast, when shock processing–driven by either jets or outflows in diverse AGN environments–becomes the dominant or a significant component of the feedback process, ionized PAHs are preferentially destroyed through shock interactions, thereby increasing the relative abundance of the surviving neutral PAHs. This mode of feedback appears to operate over more extended spatial scales in the targets examined here and is observed across a wider range of AGN types and luminosities in the literature. In particular, shocks arise from jets are more commonly associated with LINERs (see e.g., Zhang et al. 2026), whereas shocks driven by outflows are also frequently observed in Seyfert galaxies (see e.g., García-Bernete et al. 2024b). These results are consistent with the conclusions of Zhang et al. (2022), who showed that the relatively low PAH 6.2/7.7 and elevated PAH 11.3/7.7 ratios observed in spatially resolved $10''$ scale spaxels across a sample of 30 nearby AGN with $\log L_{\rm bol}/{\rm erg\,s^{-1}} \approx 39.0-42.5$ cannot be attributed solely to the AGN radiation field, but instead point to the combined influence of AGN radiation fields and shocks. The above results point to a unified framework in which AGN type is not the primary factor governing the impact of AGN feedback. Rather, the underlying physical conditions–specifically the relative importance of AGN irradiation and shock processing–play a more fundamental role in determining the effectiveness of AGN feedback, and in shaping its influence on the ISM. Consistent with the unified framework proposed here, a growing number of studies combining (rest-frame) optical IFU spectroscopy with radio observations have revealed compelling evidence for the coexistence of radiative and kinetic feedback in AGN environments (e.g., Rupke & Veilleux 2011; Girdhar et al. 2022; Venturi et al. 2023; Roy et al. 2026). Collectively, these findings support a unified view of AGN feedback as a multi-channel process, in which multiple feedback mechanisms can operate simultaneously, rather than being treated as mutually exclusive modes.

Within this unified framework, the seemingly disparate results discussed in Section 3.1 can be reconciled by accounting for the differences in sample selection. Specifically, the local ($z \lesssim 0.015$) Seyfert nuclei analyzed by Diamond-Stanic & Rieke (2010) have PAH 11.3/7.7 $\approx 0.2-1.0$ and exhibit a significant positive correlation between the PAH 11.3/7.7 ratio and the H_2 $S(3)$/(PAH7.7+PAH11.3) ratio (see Figure 6 therein). Remarkably, the six nuclei with the highest H_2 $S(3)$/(PAH7.7+PAH11.3) ratios and PAH 11.3/7.7 $\gtrsim 0.6$ deviate from the PAH7.7–[Ne II]12.81 correlation, yet still follow the corresponding PAH11.3–[Ne II]12.81 correlation. This behavior led Diamond-Stanic & Rieke (2010) to conclude that the 11.3 μm PAH feature provides a more robust SFR indicator in these systems. In contrast, the slightly distant ($z \approx 0.025 - 0.1$) AGN sample presented by LaMassa et al. (2012) exhibits generally lower PAH 11.3/7.7 ratios ($\sim 0.1 - 0.4$) and a clear negative correlation between the PAH EW11.3, as well as the PAH 11.3/7.7 ratio, and the [Ne V]14.32/[Ne II]12.81 ratio (see Figures 7 and 10 therein). Furthermore, the PAH EW11.3 values ($\lesssim 0.35$) of the local Seyfert nuclei studied by Esquej et al. (2014) lie within the regime where the negative [Ne V]14.32/[Ne II]12.81–PAH EW11.3 correlation reported by LaMassa et al. (2012) starts to flatten at the high [Ne V]14.32/[Ne II]12.81 end. Within the unified framework, the AGN samples studied by Diamond-Stanic & Rieke (2010) and LaMassa et al. (2012) predominantly trace the two feedback regimes dominated by shock processing and AGN irradiation, respectively, with the former preferentially producing weaker PAH 7.7 μm feature and the latter preferentially producing weaker PAH 11.3 μm feature. Moreover, the generally higher redshifts and larger fraction of ionized PAHs in the AGN sample presented by LaMassa et al. (2012) are consistent with stronger radiative-mode AGN feedback at higher redshifts. Supporting this interpretation, Lofaro et al. (2026) recently found from their JWST spectroscopy that the only AGN-hosting galaxy in the PAHSPECS sample of five star-forming galaxies at $z \approx 1.1$ exhibits PAH 6.2/7.7 ≈ 0.13 and 11.3/7.7 ≈ 0.16 (extinction corrected), indicative of radiative-mode AGN feedback. In contrast, the four purely star-forming galaxies have PAH 6.2/7.7 ≈ 0.33 and 11.3/7.7 ≈ 0.1–0.3, values more consistent with those measured in the resolved star-forming spaxels of local galaxies (see also Donnan et al. 2026 for spatially resolved analysis of the same PAHSPECS sample). The reconciliation of these disparate results within this unified framework further validates its robustness and highlights the fundamental role of the underlying physical conditions–especially the relative contributions of AGN irradiation and shock processing–in governing the manifestation and effectiveness of AGN feedback.

Beyond the two distinct trends of progressive PAH modifications associated with the two primary modes of AGN feedback, several higher-order variations also merit discussion. As discussed by Zhang et al. (2024b, 2026), shocks may also contribute to the production of smaller PAHs through the shattering and fragmentation of larger grains in highly obscured regions, where the resulting small PAHs can be effectively shielded from subsequent photodestruction (e.g., Alonso-Herrero et al. 2014, 2020; García-Bernete et al. 2022b, 2026). This process helps explain the enhancement of both PAH 6.2/7.7 and 11.3/7.7 ratios observed in the nuclei of NGC 1097 and throughout NGC 4736, and likely also in the lower corners of panels (a5) and (b5) in Figures 3, which spatially coincide with the terminus of one of the spiraling gas arms feeding the circumnuclear disk in Circinus (e.g., Izumi et al. 2018; Goesaert et al. 2025). An alternative scenario, particularly for the (post-)starburst systems NGC 4736 and Circinus, is that the spaxels with larger PAH 6.2/7.7 ratios–indicating a higher fraction of small PAHs–reflect the bottom-up formation of PAHs from evolved stars. This interpretation is consistent with their comparatively enhanced PAH emission relative to the other three targets (see Figure 1), although the contribution of evolved stars to PAH production remains debated (for a review see Li 2020). Nevertheless, the starburst nature of the nuclear region in Circinus, with $\Sigma_{\rm SFR}$ of $10\,M_\odot\,{\rm yr}^{-1}\,{\rm kpc}^{-2}$ (see Figure 1 and also For et al. 2012), likely contributes to the ionization of PAHs, helping to explain the most extreme ionization fraction observed in this galaxy (see also Yui Dan et al. 2026 for a similar distribution of PAH band ratios among spatially resolved spaxels in an AGN–starburst composite). In particular, the $\rm rH_2$ values of most spaxels in Circinus are consistent with a significant contribution from star-formation activity to the excitation of H_2 (see Figure A1), although ionized emission-line diagnostics indicate that all spaxels in Circinus are dominated by AGN excitation (see Figure A2). We also note that NGC 1097 hosts a starburst ring at $r \approx 7 - 10''$, whereas the central $r \lesssim 2''$ region studied here is dominated by AGN activity (e.g., Hummel et al. 1987; Hsieh et al. 2011; Mezcua & Prieto 2014; Tabatabaei et al. 2018), consistent with the relatively suppressed PAH emission observed in the nuclear region of this target (see Figure 1). Therefore, the enhanced PAH 6.2/7.7 and PAH 11.3/7.7 ratios observed in the nucleus of NGC 1097 are more likely explained by the former scenario, although we cannot entirely rule out the inward migration of newly formed PAHs from the starburst ring.

4.3. *Applications in Quantifying AGN Feedback*

The above sections propose a unified framework for interpreting two distinct modes of AGN feedback operating in the central regions of AGN, highlighting the critical role of spatially resolved analysis for disentangling these feedback processes. In Section 3.1, we discuss the practical application of our results in calibrating SFRs from PAH emission in AGN. In Section 3.2, our findings highlight the strong potential of PAH features not only as tracers of SFRs, but also as quantitative diagnostics of AGN feedback, analogous to the role of traditional BPT diagrams in probing excitation mechanisms. Moreover, the results presented above suggest that AGN irradiation is preferentially associated with AGN ionization cones, whereas shock processing associated with either jets or outflows exhibits a broader spatial distribution and operates across a wider range of environments, including both LINERs and Seyfert galaxies. Developing this unified framework into a more rigorous quantitative one, including the establishment of anchor points for quantifying the relative contributions of different AGN feedback modes and the construction of a mixing-sequence PAH diagram to trace their interplay, will require extending the present analysis to a larger AGN sample that more comprehensively covers the full range of AGN luminosities and shock strengths.

Such a more rigorous quantitative framework, to be developed in future work, holds considerable promise for quantifying the relative impact of different AGN feedback modes in observations and thereby refining prescriptions for AGN-driven energy injection into the surrounding ISM in cosmological simulations. Specifically, this analysis has the potential to provide constraints for the structure and energetics of the AGN central engine in subgrid simulations, particularly when informed by observational constraints spanning a wide range of AGN luminosities and shock strengths. Theoretical studies indicate that AGN may operate in distinct accretion modes, from radiatively efficient, geometrically thin disks at high Eddington ratios to radiatively inefficient, geometrically thick flows at low accretion rates, which in turn regulate the balance between radiative and kinetic feedback (for reviews see Yuan & Narayan 2014; Heckman & Best 2014). These differences are expected to leave measurable imprints on the surrounding ISM, as observed in the PAH features, which can in turn provide constraints on the structure and energetics of the AGN central engine. In contrast to the more concentrated distribution of ionized emission-line ratios in the targets studied here (see Figure A2), the broader and more continuous distribution of PAH band ratios suggests that PAH features more effectively trace the nonhomogeneous feedback processings associated with different AGN central engines, rather than the more general radiation-field strength traced by ionized emission lines.

JWST IFU spectroscopy also provides an opportunity to better constrain AGN duty cycles using tracers with complementary response timescales to nuclear activity. As discussed above, PAH molecules in AGN environments are vulnerable to destruction by feedback processings, and studies have estimated their lifetimes therein to be on the order of $\sim 10^3$–10^5 yr (Voit 1992; Micelotta et al. 2010b). These timescales are intermediate between the near-instantaneous response of high-ionization coronal lines, and the longer dynamical timescales of large-scale multiphase outflows ($\gtrsim 10^6$ yr; for a review see Veilleux et al. 2005). Consequently, the spatially resolved distributions of PAH emission, coronal line strengths, and multiphase outflow kinematics–all accessible in the infrared–provide temporally sensitive probes of recent AGN activity, enabling the reconstruction of episodic accretion histories and tighter constraints on AGN lifetimes and duty cycles in subgrid prescriptions for cosmological simulations. These applications further demonstrate the potential of this unified framework for future studies to quantify the impact of AGN feedback and constrain the spatial and temporal scales over which different feedback modes operate.

5. SUMMARY

Using high-quality JWST MIRI/MRS IFU spectroscopy as part of the Galaxy Activity, Torus, and Outflow Survey (GATOS), this manuscript presents a spatially resolved analysis of diagnostic features from ionized gas, H_2, and PAHs in the central $r \approx 40 - 240$ pc regions of five carefully selected AGN. The sample consists of two Seyfert galaxies for which JWST spectroscopic observations are presented here for the first time, and three LINERs for which only nuclear integrated spectra have previously been analyzed. The observations probe physical scales of $\sim 4 - 24$ pc across the sample spanning nearly four orders of magnitude in AGN luminosity ($\log L_{\rm bol}/{\rm erg\,s^{-1}} \approx 39.8 - 43.8$).

By combining measurements of the relative suppression of individual PAH features, the bimodal distributions of PAH band ratios, and tracers of shock processing and AGN irradiation, we identify two distinct AGN feedback modes that imprint characteristic signatures on PAH properties, associated with shock processing and AGN irradiation, respectively. These modes broadly correspond to the kinetic (or radio) and radiative (or quasar) forms of AGN feedback, underscoring the diagnostic power of PAH emission for probing AGN feedback processes. The spatially resolved analysis further reveals that the kinetic and radiative modes of AGN feedback can coexist in the central regions of AGN, although one mode generally dominates. Moreover, AGN irradiation appears to be preferentially associated with AGN ionization cones and is likely to become more important at higher redshifts. In contrast, shock processing–driven by either jets or outflows–exhibits a broader spatial distribution and is widespread among local AGN, including both LINERs and Seyfert galaxies.

The findings from the spatially resolved analysis provide new insights into calibrating SFRs from PAH emission in AGN and, more importantly, into distinguishing between different modes of AGN feedback. Together, the results and discussions presented here point to a practical unified framework for AGN feedback that incorporates both AGN irradiation and shock processing, enabling future investigations to quantify their relative contributions and constrain the spatial and temporal scales over which distinct feedback modes operate. This framework has the potential to provide critical observational benchmarks for modeling AGN-driven galaxy evolution, including constraints on the structure and energetics of the AGN central engine in subgrid simulations across a wide range of luminosities, as well as on AGN duty cycles through tracers with complementary response timescales to AGN activity.

ACKNOWLEDGMENTS

We thank the anonymous referee for the constructive and insightful comments, which have significantly improved the clarity and presentation of this manuscript.

We thank Xiwen Zhu for assistance in preparing the schematic illustration presented in Figure 6. LZ and CP acknowledge grant support from the Space Telescope Science Institute (ID: JWST-GO-01670; JWST-GO-03535; JWST-GO-04225; JWST-GO-04972; JWST-GO-07429). EKSH and DD acknowledge support from the NASA Astrophysics Data Analysis Program (22-ADAP22-0173). OG-M acknowledge financial support from PAPIIT/DGAPA UNAM project IN109123, Ciencia de Frontera SECIHTI project CF-2023-G100, and sabbatical grant by PASPA/GDAPA at UNAM. RAR acknowledges the support from the Conselho Nacional de Desenvolvimento Científico e Tecnológico (CNPq; Projects 303450/2022-3, and 403398/2023-1), the Coordenação de Aperfeiçoamento de Pessoal de Nível Superior (CAPES; Project 88887.894973/2023-00), and Fundação de Amparo à Pesquisa do Estado do Rio Grande do Sul (FAPERGS; Project 25/2551-0002765-9). MPS acknowledges support from grants RYC2021-033094-I, CNS2023-145506, and PID2023-146667NB-I00 funded by MCIN/AEI/10.13039/501100011033 and the European Union NextGenerationEU/PRTR. AJB acknowledges funding from the "FirstGalaxies" Advanced Grant from the European Research Council (ERC) under the European Union's Horizon 2020 research and innovation program (Grant agreement No. 789056). EB cknowledge funding from the TEC-2024/TEC-182 project funded by the Comunidad de Madrid and from the grant PID2022-138621NB-I00, funded by MCIN/AEI/10.13039/501100011033/FEDER, EU. AA is funded by the European Union (Widening Participation, ExGal-Twin, GA 101158446.

REFERENCES

Aitken, D. K. & Roche, P. F. 1985, MNRAS, 213, 777
Alexander, D. M. & Hickox, R. C. 2012, NewAR, 56, 4, 93
Allain, T., Leach, S., & Sedlmayr, E. 1996, A&A, 305, 616
Allen, M. G., Groves, B. A., Dopita, M. A., et al. 2008, ApJS, 178, 1, 20
Alonso-Herrero, A., García-Burillo, S., Hönig, S. F., et al. 2021, A&A, 652, A99
Alonso Herrero, A., Hermosa Muñoz, L., Labiano, A., et al. 2025, A&A, 699, A334
Alonso-Herrero, A., Pereira-Santaella, M., Rigopoulou, D., et al. 2020, A&A, 639, A43
Alonso-Herrero, A., Ramos Almeida, C., Esquej, P., et al. 2014, MNRAS, 443, 2766
Annuar, A., Alexander, D. M., Gandhi, P., et al. 2025, MNRAS, 540, 4, 3827
Argyriou, I., Glasse, A., Law, D. R., et al. 2023, A&A, 675, A111
Audibert, A., Ramos Almeida, C., García-Burillo, S., et al. 2023, A&A, 671, L12
Bellocchi, E., Longinotti, A. L., Salomé, Q., et al. 2026, A&A, 709, A260
Bierschenk, M., Ricci, C., Temple, M. J., et al. 2024, ApJ, 976, 2, 257
Bushouse, H., Eisenhamer, J., Dencheva, N., et al. 2025, Zenodo, 1.18.0. doi:10.5281/zenodo.15178003
Chown, R., Okada, Y., Peeters, E., et al. 2025, A&A, 698, A86.
Cicone, C., Maiolino, R., Sturm, E., et al. 2014, A&A, 562, A21
Cisternas, M., Gadotti, D. A., Knapen, J. H., et al. 2013, ApJ, 776, 1, 50
Colina, L., Piqueras López, J., Arribas, S., et al. 2015, A&A, 578, A48
Cortzen, I., Garrett, J., Magdis, G., et al. 2019, MNRAS, 482, 2, 1618
Costa-Souza, J. H., Colina, L., Riffel, R. A., et al. 2026, arXiv:2605.04925
Crain, R. A., Schaye, J., Bower, R. G., et al. 2015, MNRAS, 450, 2, 1937
da Silva, P., Menezes, R. B., Díaz, Y., et al. 2023, MNRAS, 519, 1, 1293
Dasyra, K. M., Paraschos, G. F., Combes, F., et al. 2024, ApJ, 977, 2, 156
Davé, R., Crain, R. A., Stevens, A. R. H., et al. 2020, MNRAS, 497, 1, 146
Davies, R. I., Maciejewski, W., Hicks, E. K. S., et al. 2014, ApJ, 792, 2, 101
Davies, R., Shimizu, T., Pereira-Santaella, M., et al. 2024, A&A, 689, A263
Delaney, D. E., Hicks, E. K. S., Zhang, L., et al. 2026, ApJ, 1002, 1, 20
Di Matteo, T., Springel, V., & Hernquist, L. 2005, Nature, 433, 7026, 604
Diamond-Stanic, A. M. & Rieke, G. H. 2010, ApJ, 724, 140
Dors, O. L., Riffel, R. A., Cardaci, M. V., et al. 2012, MNRAS, 422, 1, 252
Donnan, F. R., García-Bernete, I., Rigopoulou, D., et al. 2024, MNRAS, 529, 2, 1386
Donnan, F. R., Sandstrom, K., Shivaei, I., et al. 2026, MNRAS, in press, arXiv:2606.18244
Dopita, M. A., Ho, I.-T., Dressel, L. L., et al. 2015, ApJ, 801, 1, 42
Draine, B. T. & Li, A. 2007, ApJ, 657, 810
Draine, B. T., Li, A., Hensley, B. S., et al. 2021, ApJ, 917, 3

Durré, M. & Mould, J. 2018, ApJ, 867, 2, 149

Greene, J. E., Strader, J., & Ho, L. C. 2020, ARA&A, 58, 257

Esparza-Arredondo, D., González-Martín, O., Dultzin, D., et al. 2018, ApJ, 859, 2, 124

Esposito, F., Alonso-Herrero, A., García-Burillo, S., et al. 2024, A&A, 686, A46

Esquej, P., Alonso-Herrero, A., González-Martín, O., et al. 2014, ApJ, 780, 1, 86

Fabian, A. C. 2012, ARA&A, 50, 455

Fernández-Ontiveros, J. A., Prieto, M. A., Acosta-Pulido, J. A., et al. 2012, Journal of Physics Conference Series, 372, 1, 012006

Fiore, F., Feruglio, C., Shankar, F., et al. 2017, A&A, 601, A143

Fluetsch, A., Maiolino, R., Carniani, S., et al. 2019, MNRAS, 483, 4, 4586

For, B.-Q., Koribalski, B. S., & Jarrett, T. H. 2012, MNRAS, 425, 3, 1934

Forbes, D. A. & Ward, M. J. 1993, ApJ, 416, 150

Foreman-Mackey, D., Hogg, D. W., Lang, D., et al. 2013, PASP, 125, 925, 306

García-Bernete, I., Pereira-Santaella, M., González-Alfonso, E., et al. 2026, Nature Astronomy, 10, 420

García-Bernete, I., Ramos Almeida, C., Acosta-Pulido, J. A., et al. 2015, MNRAS, 449, 2, 1309

García-Bernete, I., Ramos Almeida, C., Landt, H., et al. 2017, MNRAS, 469, 1, 110

García-Bernete, I., Rigopoulou, D., Alonso-Herrero, A., et al. 2022a, A&A, 666, L5

García-Bernete, I., Rigopoulou, D., Alonso-Herrero, A., et al. 2022b, MNRAS, 509, 4256

García-Bernete, I., Rigopoulou, D., Donnan, F. R., et al. 2024b, A&A, 691, A162

García-Burillo, S., Alonso-Herrero, A., Ramos Almeida, C., et al. 2021, A&A, 652, A98

García-Burillo, S., Hicks, E. K. S., Alonso-Herrero, A., et al. 2024, A&A, 689, A347

Gardner, J. P., Mather, J. C., Abbott, R., et al. 2023, PASP, 135, 1048, 068001

Girdhar, A., Harrison, C. M., Mainieri, V., et al. 2022, MNRAS, 512, 2, 1608

Goesaert, W. M., Tristram, K. R. W., Impellizzeri, C. M. V., et al. 2025, A&A, 704, A125

Goold, K., Seth, A., Molina, M., et al. 2024, ApJ, 966, 2, 204

Goold, K., Seth, A., Molina, M., et al. 2026, ApJ, 1000, 2, 281

Guillard, P., Boulanger, F., Pineau Des Forêts, G., et al. 2009, A&A, 502, 2, 515

Guillard, P., Ogle, P. M., Emonts, B. H. C., et al. 2012, ApJ, 747, 95

Harrison, C. M. & Ramos Almeida, C. 2024, Galaxies, 12, 2, 17

Heckman, T. M. & Best, P. N. 2014, ARA&A, 52, 589

Hermosa Muñoz, L., González Fernández, J. R., Alonso-Herrero, A., et al. 2026, A&A, 708, A297

Ho, L. C. 2008, ARA&A, 46, 475

Ho, L. C. 2009, ApJ, 699, 1, 626

Ho, L. C., Filippenko, A. V., & Sargent, W. L. W. 2003, ApJ, 583, 1, 159

Ho, L. C., Greene, J. E., Filippenko, A. V., et al. 2009, ApJS, 183, 1, 1

Hollenbach, D. & McKee, C. F. 1989, ApJ, 342, 306

Holm, A. I. S., Johansson, H. A. B., Cederquist, H., et al. 2011, JChPh, 134, 4, 044301

Hopkins, P. F., Hernquist, L., Cox, T. J., et al. 2008, ApJS, 175, 2, 356

Hsieh, P.-Y., Matsushita, S., Liu, G., et al. 2011, ApJ, 736, 2, 129

Hummel, E., van der Hulst, J. M., & Keel, W. C. 1987, A&A, 172, 32

Izumi, T., Wada, K., Fukushige, R., et al. 2018, ApJ, 867, 1, 48

Jensen, J. J., Hönig, S. F., Rakshit, S., et al. 2017, MNRAS, 470, 3, 3071

Kennicutt, R. C., Armus, L., Bendo, G., et al. 2003, PASP, 115, 810, 928

Kristensen, L. E., Godard, B., Guillard, P., et al. 2023, A&A, 675, A86

Koo, B.-C., Raymond, J. C., & Kim, H.-J. 2016, Journal of Korean Astronomical Society, 49, 3, 109

Kormendy, J. & Ho, L. C. 2013, ARA&A, 51, 1, 511

Lai, T. S.-Y., Armus, L., U, V., et al. 2022, ApJL, 941, 2, L36

LaMassa, S. M., Heckman, T. M., Ptak, A., et al. 2012, ApJ, 758, 1, 1

Law, D. R., E. Morrison, J., Argyriou, I., et al. 2023, AJ, 166, 2, 45

Leroy, A. K., Sandstrom, K., Rosolowsky, E., et al. 2023, ApJL, 944, 2, L9

Lofaro, C. M., Díaz Santos, T., Shivaei, I., et al. 2026, arXiv:2606.18230

Li, A. 2020, Nature Astronomy, 4, 339

López, I. E., Bertola, E., Reynaldi, V., et al. 2025, A&A, 704, A88

Lopez-Rodriguez, E., Sanchez-Bermudez, J., González-Martín, O., et al. 2026, Nature Communications, 17, 1, 42

Maragkoudakis, A., Boersma, C., Peeters, E., et al. 2026, A&A, 709, A38

Maragkoudakis, A., Boersma, C., Temi, P., et al. 2025, ApJ, 979, 1, 90

Maragkoudakis, A., Ivkovich, N., Peeters, E., et al. 2018, MNRAS, 481, 5370

Marconi, A., Moorwood, A. F. M., Origlia, L., et al. 1994, The Messenger, 78, 20

Marshall, J. A., Herter, T. L., Armus, L., et al. 2007, ApJ, 670, 1, 129

McNamara, B. R. & Nulsen, P. E. J. 2007, ARA&A, 45, 1, 117

Mezcua, M. & Prieto, M. A. 2014, ApJ, 787, 1, 62

Micelotta, E. R., Jones, A. P., & Tielens, A. G. G. M. 2010a, A&A, 510, A36
Micelotta, E. R., Jones, A. P., & Tielens, A. G. G. M. 2010b, A&A, 510, A37
Morganti, R., Fogasy, J., Paragi, Z., et al. 2013a, Science, 341, 6150, 1082
Morganti, R., Frieswijk, W., Oonk, R. J. B., et al. 2013b, A&A, 552, L4
Mouri, H., Kawara, K., & Taniguchi, Y. 2000, ApJ, 528, 1, 186
Nagar, N. M., Falcke, H., & Wilson, A. S. 2005, A&A, 435, 2, 521
Nemmen, R. S., Storchi-Bergmann, T., & Eracleous, M. 2014, MNRAS, 438, 4, 2804
Nesvadba, N. P. H., Drouart, G., De Breuck, C., et al. 2017, A&A, 600, A121
O'Dowd, M. J., Schiminovich, D., Johnson, B. D., et al. 2009, ApJ, 705, 885
Ogle, P., Boulanger, F., Guillard, P., et al. 2010, ApJ, 724, 2, 1193
Ogle, P. M., Sebastian, B., Aravindan, A., et al. 2025, ApJ, 983, 2, 98
Pantoni, L., Baes, M., Decin, L., et al. 2026, arXiv:2603.23674
Pellegrini, S., Fabbiano, G., Fiore, F., et al. 2002, A&A, 383, 1
Pillepich, A., Springel, V., Nelson, D., et al. 2018, MNRAS, 473, 3, 4077
Pontoppidan, K. M., Salyk, C., Banzatti, A., et al. 2024, ApJ, 963, 2, 158
Ramos Almeida, C., Bischetti, M., García-Burillo, S., et al. 2022, A&A, 658, A155
Ramos Almeida, C., Esparza-Arredondo, D., González-Martín, O., et al. 2023, A&A, 669, L5
Ramos Almeida, C., García-Bernete, I., Pereira-Santaella, M., et al. 2025, A&A, 698, A194
Richings, A. J. & Faucher-Giguère, C.-A. 2018a, MNRAS, 478, 3, 3100
Richings, A. J. & Faucher-Giguère, C.-A. 2018b, MNRAS, 474, 3, 3673
Riffel, R. A., Bianchin, M., Riffel, R., et al. 2021, MNRAS, 503, 4, 5161
Riffel, R. A., Colina, L., Costa-Souza, J. H., et al. 2026a, A&A, 705, A59
Riffel, R. A., Souza-Oliveira, G. L., Colina, L., et al. 2026b, arXiv:2605.02663
Riffel, R. A., Zakamska, N. L., & Riffel, R. 2020, MNRAS, 491, 1, 1518
Rigopoulou, D., Barale, M., Clary, D. C., et al. 2021, MNRAS, 504, 5287
Rigopoulou, D., Donnan, F. R., García-Bernete, I., et al. 2024, MNRAS, 532, 2, 1598
Roche, P. F., Packham, C., Telesco, C. M., et al. 2006, MNRAS, 367, 4, 1689
Rodríguez-Ardila, A., Mason, R. E., Martins, L., et al. 2017, MNRAS, 465, 1, 906
Roussel, H., Helou, G., Hollenbach, D. J., et al. 2007, ApJ, 669, 959
Roy, N., Heckman, T., Henry, A., et al. 2026, ApJ, 1002, 1, 57
Rupke, D. S. N. & Veilleux, S. 2011, ApJL, 729, 2, L27
Sales, D. A., Pastoriza, M. G., & Riffel, R. 2010, ApJ, 725, 605
Seabold, S., & Perktold, J. 2010, in Proc. of the 9th Python 558 in Science Conf., ed. S. van der Walt & J. Millman (Austin, TX: Enthought, Inc.), 92
Shipley, H. V., Papovich, C., Rieke, G. H., et al. 2016, ApJ, 818, 60
Silk, J. & Rees, M. J. 1998, A&A, 331, L1
Smith, J. D. T., Draine, B. T., Dale, D. A., et al. 2007, ApJ, 656, 2, 770
Storchi-Bergmann, T., McGregor, P. J., Riffel, R. A., et al. 2009, MNRAS, 394, 3, 1148
Tabatabaei, F. S., Minguez, P., Prieto, M. A., et al. 2018, Nature Astronomy, 2, 83
Thean, A., Pedlar, A., Kukula, M. J., et al. 2000, MNRAS, 314, 3, 573
Tielens, A. G. G. M. 2008, ARA&A, 46, 289
Togi, A. & Smith, J. D. T. 2016, ApJ, 830, 18
Treyer, M., Schiminovich, D., Johnson, B. D., et al. 2010, ApJ, 719, 1191
Van De Putte, D., Peeters, E., Gordon, K. D., et al. 2025, A&A, 701, A111
Veilleux, S., Cecil, G., & Bland-Hawthorn, J. 2005, ARA&A, 43, 1, 769
Venturi, G., Cresci, G., Marconi, A., et al. 2021, A&A, 648, A17
Venturi, G., Treister, E., Finlez, C., et al. 2023, A&A, 678, A127
Voit, G. M. 1992, MNRAS, 258, 841
Weaver, K. A., Meléndez, M., Mushotzky, R. F., et al. 2010, ApJ, 716, 2, 1151
Weinberger, R., Springel, V., Hernquist, L., et al. 2017, MNRAS, 465, 3, 3291
Wells, M., Pel, J.-W., Glasse, A., et al. 2015, PASP, 127, 953, 646
Wright, G. S., Rieke, G. H., Glasse, A., et al. 2023, PASP, 135, 1046, 048003
Xie, Y. & Ho, L. C. 2019, ApJ, 884, 136
Xie, Y. & Ho, L. C. 2022, ApJ, 925, 218
Yuan, F. & Narayan, R. 2014, ARA&A, 52, 529
Yui Dan, K., Seebeck, J., Veilleux, S., et al. 2026, arXiv:2605.03016
Zhang, L. & Ho, L. C. 2023a, ApJ, 943, 1, 1
Zhang, L. & Ho, L. C. 2023b, ApJ, 943, 1, 60
Zhang, L. & Ho, L. C. 2023c, ApJL, 953, 1, L9
Zhang, L., Davies, R. I., Packham, C., et al. 2025, ApJS, 280, 2, 65
Zhang, L., García-Bernete, I., Packham, C., et al. 2024b, ApJL, 975, 1, L2
Zhang, L., Ho, L. C., & Li, A. 2022, ApJ, 939, 22

Zhang, L., Packham, C., Hicks, E. K. S., et al. 2024a, ApJ, 974, 2, 195

Zhang, L., Packham, C., Hicks, E. K. S., et al. 2026, ApJL, 998, 2, L32

Zhuang, M.-Y., Ho, L. C., & Shangguan, J. 2019, ApJ, 873, 2, 103

APPENDIX

A. SUPPLEMENTARY FIGURES

See Figures A1 and A2 for the diagnostic diagram of [Ne V]14.32/PAH11.3 vs H_2 $S(1–5)$/PAH7.7 and the diagnostic diagrams of: (a) [Ne V]/[Ne III] vs. [O IV]/[Ne III] and (b) [Ne V]/[Ne III] vs. [Fe II]/[Ar II], respectively. See Figure A3 for the PAH 11.3/6.2 versus PAH 6.2/7.7 diagnostic diagram, and see Figure A4 for examples illustrating the multi-component fitting procedure used to measure the PAH features. See Tables A1 and A2 for the corresponding coefficients in Equations 1 and 2, respectively. See Table A3 for the flux measurements of the PAH 6.2, 7.7, and 11.3 μm features; the H_2 $S(1)$–$S(6)$ transitions; and the [Ne II]12.81μm, [Ne III]15.555μm, [Ne V]14.32μm, [Fe II]5.34μm, and [Ar II]6.985μm emission lines measured from the aperture-extracted spectra shown in Figure A4.

Table A1. Coefficients in Equation 1

Feature	α_1	α_2	α_3	β	σ (dex)
(1)	(2)	(3)	(4)	(5)	(6)
PAH6.2	0.87±0.02	−0.90±0.03	−0.26±0.01	38.68±0.12	0.25
PAH7.7	0.88±0.01	−0.86±0.02	−0.19±0.01	39.60±0.10	0.19
PAH11.3	0.78±0.02	−0.64±0.02	−0.32±0.01	38.59±0.11	0.21

Table A2. Coefficients in Equation 2

Feature	α_1	α_2	α_3	β	σ (dex)
(1)	(2)	(3)	(4)	(5)	(6)
PAH6.2	0.83±0.02	0.50±0.03	0.25±0.01	−34.05±0.54	0.24
PAH7.7	0.93±0.01	0.63±0.03	0.20±0.01	−38.04±0.47	0.20
PAH11.3	0.94±0.02	0.38±0.03	0.34±0.01	−38.25±0.60	0.24

Table A3. Flux Measurements from Aperture-extracted Spectra

Aperture	$\log f_{\rm PAH}^{6.2}$	$\log f_{\rm PAH}^{7.7}$	$\log f_{\rm PAH}^{11.3}$	$\log f_{\rm H_2}^{S(1)}$	$\log f_{\rm H_2}^{S(2)}$	$\log f_{\rm H_2}^{S(3)}$	$\log f_{\rm H_2}^{S(4)}$	$\log f_{\rm H_2}^{S(5)}$	$\log f_{\rm H_2}^{S(6)}$	$\log f_{\rm [Ne\,II]}^{12.81}$	$\log f_{\rm [Ne\,III]}^{15.56}$	$\log f_{\rm [Ne\,V]}^{14.32}$	$\log f_{\rm [Fe\,II]}^{5.34}$	$\log f_{\rm [Ar\,II]}^{6.99}$	$\log \tau_{9.7}$
(1)	(2)	(3)	(4)	(5)	(6)	(7)	(8)	(9)	(10)	(11)	(12)	(13)	(14)	(15)	(16)
NGC1097_0.5	−13.20±0.07	−12.74±0.06	−12.99±0.08	−14.08±0.01	−14.21±0.01	−14.03±0.01	−14.34±0.01	−14.09±0.01	−14.77±0.01	−13.90±0.04	−14.21±0.03	−15.39±0.03	−14.58±0.01	−14.34±0.05	−9.99
NGC1097_1.0	−13.14±0.03	−12.44±0.03	−12.86±0.04	−13.81±0.01	−13.99±0.01	−13.84±0.01	−14.19±0.01	−13.95±0.01	−14.61±0.01	−13.90±0.01	−14.21±0.02	−15.73±0.11	−14.52±0.01	−14.40±0.03	−8.49
NGC1097_1.5	−13.26±0.06	−12.48±0.05	−12.87±0.05	−13.81±0.02	−14.07±0.02	−13.92±0.01	−14.34±0.01	−14.10±0.01	−14.75±0.01	−13.97±0.18	−14.28±0.01	−16.51±0.08	−14.68±0.01	−14.59±0.12	−9.99
NGC3190_0.5	−13.79±0.05	−13.00±0.05	−13.26±0.04	−14.50±0.01	−14.61±0.01	−14.22±0.01	−14.58±0.01	−14.25±0.01	−14.91±0.01	−14.11±0.03	−14.25±0.01	−15.67±0.01	−14.55±0.01	−14.53±0.03	−0.88
NGC3190_1.0	−13.51±0.06	−12.85±0.05	−12.94±0.05	−14.22±0.01	−14.35±0.01	−14.00±0.01	−14.35±0.02	−14.02±0.01	−14.71±0.02	−13.93±0.06	−14.07±0.02	−15.74±0.01	−14.32±0.01	−14.36±0.03	−7.98
NGC3190_1.5	−13.34±0.03	−12.69±0.02	−12.78±0.01	−14.15±0.02	−14.39±0.03	−14.09±0.03	−14.49±0.03	−14.17±0.03	−14.96±0.04	−13.98±0.09	−14.14±0.08	−16.00±0.03	−14.40±0.01	−14.41±0.05	−7.88
NGC4736_0.5	−13.05±0.06	−12.65±0.05	−12.68±0.05	−14.36±0.01	−14.54±0.01	−14.15±0.01	−14.58±0.01	−14.22±0.01	−14.91±0.04	−14.38±0.01	−14.41±0.03	−15.89±0.02	−14.31±0.01	−14.60±0.05	−7.99
NGC4736_1.0	−12.67±0.06	−12.13±0.05	−12.32±0.06	−13.98±0.01	−14.21±0.02	−13.88±0.01	−14.36±0.02	−14.03±0.01	−14.76±0.04	−14.17±0.01	−14.17±0.08	−15.64±0.01	−14.08±0.01	−14.38±0.04	−7.98
NGC4736_1.5	−12.49±0.03	−11.97±0.02	−12.13±0.03	−13.77±0.02	−14.06±0.02	−13.76±0.02	−14.29±0.01	−13.96±0.01	−14.71±0.03	−14.09±0.01	−14.09±0.04	−15.66±0.01	−14.00±0.01	−14.30±0.04	−7.90
NGC7314_0.5	−13.41±0.12	−12.24±0.04	−13.15±0.08	−14.38±0.03	−14.62±0.03	−14.37±0.04	−14.66±0.02	−14.37±0.02	−15.47±0.21	−13.37±0.10	−12.97±0.03	−12.99±0.07	−14.66±0.01	−13.68±0.01	−0.60
NGC7314_1.0	−13.27±0.06	−12.48±0.06	−13.14±0.06	−14.27±0.02	−14.58±0.02	−14.35±0.03	−14.79±0.02	−14.52±0.02	−15.34±0.08	−13.57±0.01	−13.18±0.01	−13.21±0.04	−14.73±0.01	−13.92±0.01	−0.50
NGC7314_1.5	−13.55±0.06	−12.92±0.06	−13.42±0.06	−14.45±0.02	−14.85±0.01	−14.66±0.02	−15.22±0.02	−14.97±0.02	−15.64±0.02	−14.14±0.06	−13.65±0.02	−13.80±0.03	−15.13±0.01	−14.54±0.01	−0.71
Circinus_1.0	−11.64±0.06	−10.77±0.05	−12.09±0.06	−13.74±0.02	−13.88±0.02	−13.57±0.01	−13.83±0.01	−13.51±0.01	−14.32±0.08	−12.50±0.01	−12.55±0.03	−12.59±0.08	−13.55±0.01	−12.81±0.01	0.09
Circinus_1.5	−11.24±0.07	−10.53±0.06	−11.27±0.06	−13.25±0.02	−13.35±0.02	−13.16±0.02	−13.41±0.02	−13.11±0.02	−13.98±0.11	−12.22±0.04	−12.20±0.01	−12.29±0.02	−13.19±0.01	−12.54±0.01	−0.17

NOTE—Flux measurements from integrated MIRI/MRS spectra extracted from the $r \leq 0''.5$, $0''.5 \leq r \leq 1''.0$, and $1''.0 \leq r \leq 1''.5$ regions of each target. All measurements have been corrected for dust extinction based on the fitted $\tau_{9.7}$ values listed in the last column (see Section 2.3).

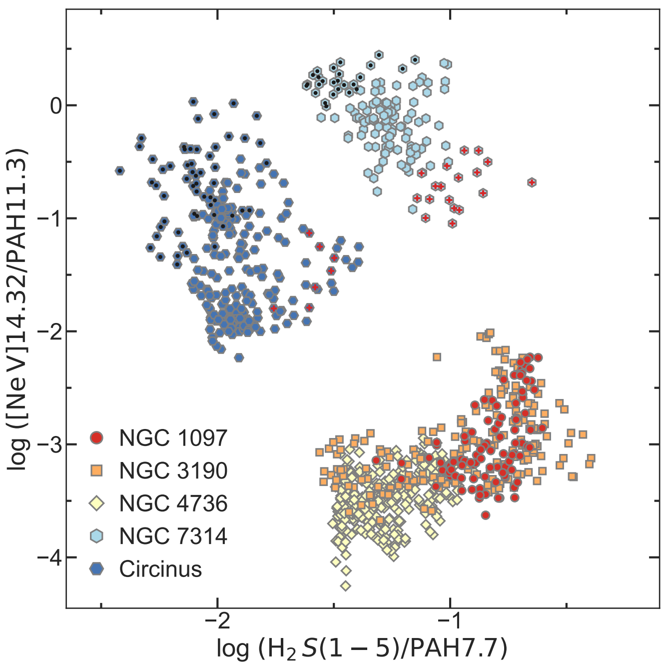

Figure A1. Diagnostic diagram of [Ne V]14.32/PAH11.3 (i.e., rNe) vs. H_2 $S(1\text{–}5)$/PAH7.7 (i.e.,rH_2) for $0\farcs2 \times 0\farcs2$ spaxels in the central $\sim 4'' \times 4''$ regions of the five AGN targets. The data points highlighted with black dots pertain to spaxels in NGC 7314 and Circinus with PAH 11.3/7.7 < 0.2 and PAH 6.2/7.7 < 0.15, while the points highlighted with red crosses pertain to those with PAH 11.3/7.7 > 0.4.

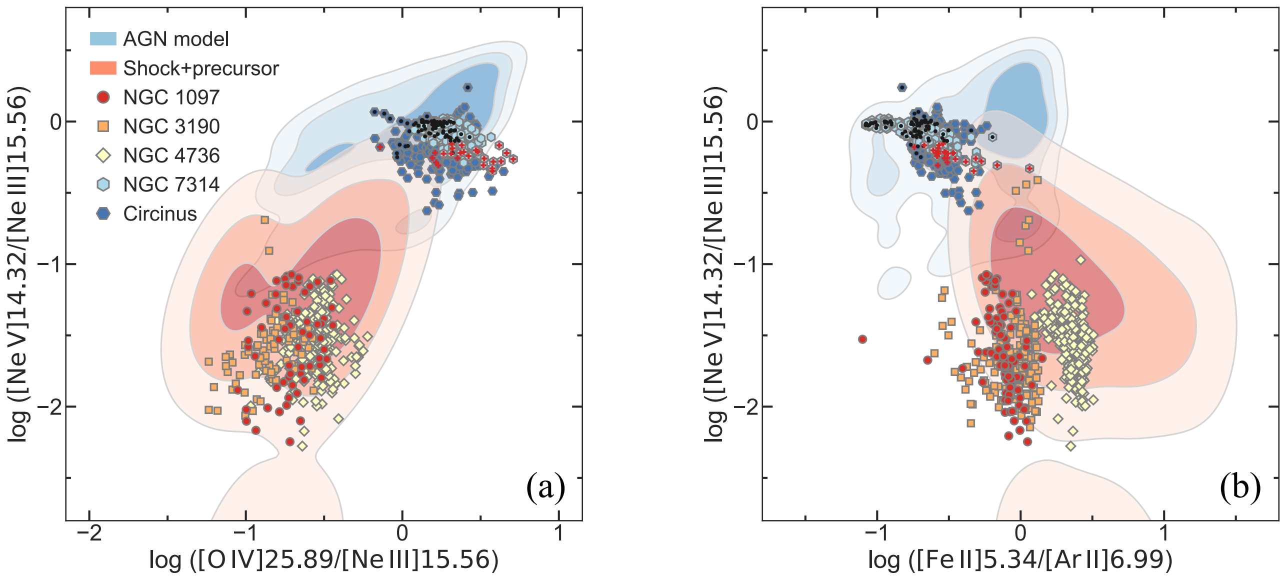

Figure A2. Diagnostic diagrams of ionized emission-line ratios: (a) [Ne V]14.32/[Ne III]15.56 vs. [O IV]25.89/[Ne III]15.56 and (b) [Ne V]14.32/[Ne III]15.56 vs. [Fe II]5.34/[Ar II]6.99 for $0''.2 \times 0''.2$ spaxels in the central $\sim 4'' \times 4''$ regions of the five AGN targets. The data points with a black dot pertain to spaxels in NGC 7314 and Circinus with PAH 11.3/7.7 < 0.2 and PAH 6.2/7.7 < 0.15, while the points with a red cross pertain to those with PAH 11.3/7.7 > 0.4. The bluish and reddish contours show the distributions of model results computed by Zhang et al. (2025) for AGN and fast radiative shocks (including the shock precursor), respectively. The included AGN models span ionization parameter $\log U$ from -2.3 to -1.8, AGN spectrum peak energy $\log\,(E_{\rm peak}/{\rm keV})$ from -2.1 to -0.9, metallicities of $1.5 - 2\,Z_\odot$, and gas pressure $\log\,(P/k)$ from 7.0 to 9.5. The included shock models cover shock velocities v_s from $100 - 400$ km s^{-1}, pre-shock density $n_{\rm H}$ from 10^3 to 10^4 cm^{-3}, magnetic to ram pressure ratio $\eta_{\rm M}$ from 0.0 to 0.001, and metallicities of $1.5 - 2\,Z_\odot$. In each case, the contours enclose 30%, 60%, and 90% of the model results, from the innermost to the outermost levels. Note that some spaxels have valid [Ne V]14.32μm measurements from Ch3 but no corresponding [O IV]25.89μm measurements from Ch4; consequently, panel (a) contains fewer data points than panel (b).

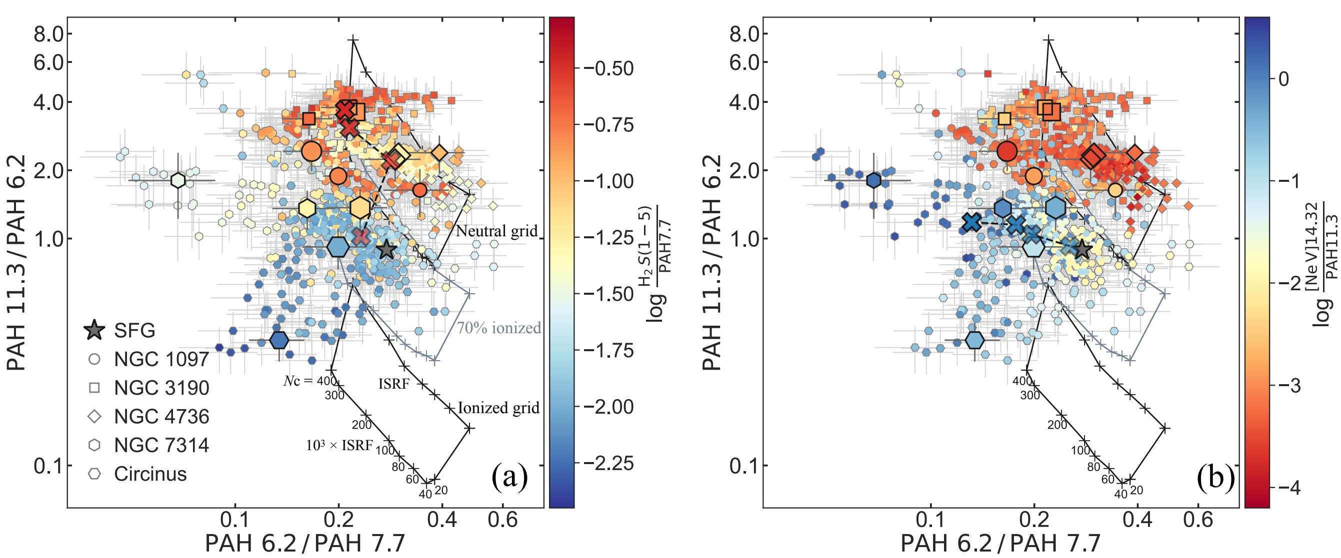

Figure A3. Same as Figure 4, but with the y-axis replaced by the PAH 11.3/6.2 ratio. In addition, the PAH band ratios derived from the integrated spectra extracted within the $r \le 0''.5$, $0''.5 \le r \le 1''.0$, and $1''.0 \le r \le 1''.5$ regions of each target are plotted with the same symbols and color coding as the spaxels in the five AGN, but are distinguished by black outlines of increasing size corresponding to the three radial apertures. Note that no data point is shown for the $r \le 0''.5$ region of Circinus, as spaxels within this aperture are affected by saturation effects (see Figure 3 and its caption).

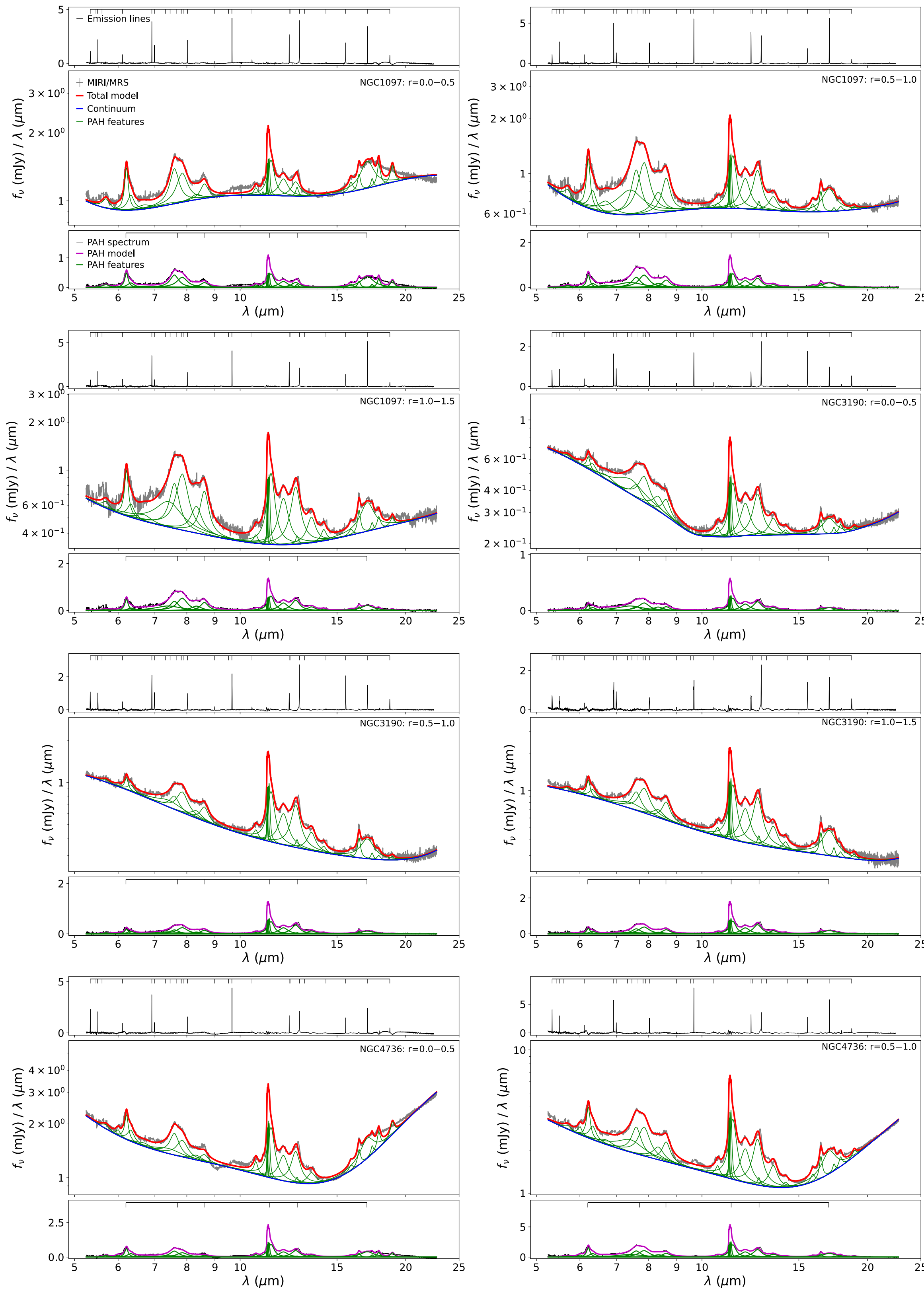
Emission lines
MIRI/MRS
Total model
Continuum
PAH features
PAH spectrum
PAH model
NGC1097: r=0.0−0.5
NGC1097: r=0.5−1.0
NGC1097: r=1.0−1.5
NGC3190: r=0.0−0.5
NGC3190: r=0.5−1.0
NGC3190: r=1.0−1.5
NGC4736: r=0.0−0.5
NGC4736: r=0.5−1.0
f_ν (mJy) / λ (μm)
λ (μm)

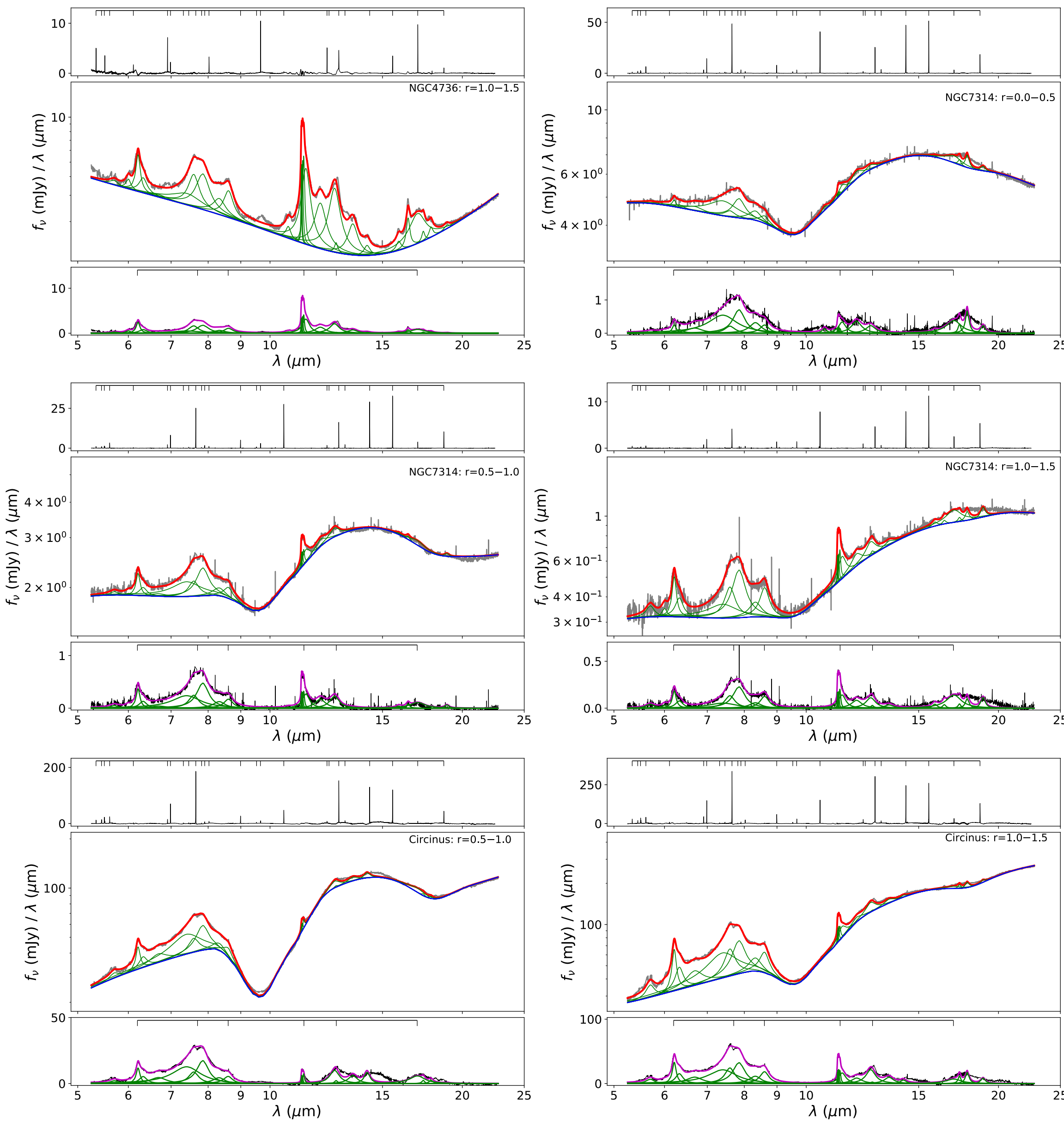

Figure A4. Top panels: Emission-line spectra obtained by subtracting the PAH emission and underlying continuum (i.e., the red curves in the middle panels) from the integrated MIRI/MRS spectra extracted from the $r \leq 0\farcs5$, $0\farcs5 \leq r \leq 1\farcs0$, and $1\farcs0 \leq r \leq 1\farcs5$ regions of each target. From left to right, the short markers at the top indicate the positions of the [Fe II]5.34μm, [Fe VIII]5.45μm, [Mg VII]5.50μm, [Mg V]5.61μm, H_2 $S(6)$, H_2 $S(5)$, [Ar II]6.985μm, [Na III]7.32μm, Pfα, [Ne VI]7.65μm, [Fe VII]7.815μm, [Ar V]7.90μm, H_2 $S(4)$, [Ar III]8.99μm, [Fe VII]9.53μm, H_2 $S(3)$, [S IV]10.51μm, H_2 $S(2)$, Huα, [Ne II]12.81μm, [Ar V]13.10μm, [Ne V]14.32μm, [Ne III]15.555μm, H_2 $S(1)$, and [S III]18.71μm emission lines, respectively. Middle panels: Illustrations of the multi-component fitting procedure used for the PAH measurements (see Section 2.3). The gray curves show the observed MIRI/MRS spectra with emission lines masked. The red curves represent the best-fit models consisting of PAH emission and the underlying continuum. The blue curves show the combined underlying continuum components (i.e., stellar and dust continua), while the green curves represent the individual PAH features modeled with Drude profiles. Bottom panels: PAH spectra (black curves) obtained by subtracting all continuum components (i.e., the blue curves in the middle panels) from the emission-line-masked MIRI/MRS spectra. As in the middle panels, the green curves represent individual PAH features modeled with Drude profiles, while the magenta curves show their sum, corresponding to the modeled PAH spectra. From left to right, the short markers at the top indicate the positions of the PAH complexes centered near 6.2, 7.7, 8.6, 11.3, 12.7, and 17.0 μm, respectively. Note that all x-axes, as well as the y-axes in the middle panels, are shown on logarithmic scales, whereas the y-axes in the top and bottom panels are shown on linear scales. No spectrum is shown for the $r \leq 0\farcs5$ region of Circinus, as noted in Figure A3.